Open access • Journal Article • DOI:10.1063/1.444862

Dynamical study of nonadiabatic unimolecular reactions: The conical intersection between the B̃ 2B2 and Ã 2A1 states of H2O+ — Source link

Dominique Dehareng, Xavier Chapuisat, Jean-Claude Lorquet, C. Galloy ...+1 more authors

Institutions: University of Liège

Published on: 01 Feb 1983 - Journal of Chemical Physics (American Institute of Physics)

Topics: Conical intersection, Diabatic, Vibronic coupling, Potential energy surface and Potential energy

Dynamical study of nonadiabatic unimolecular reactions: The conical intersection between the $\tilde{B}\,^2B_2$ and $\tilde{A}\,^2A_1$ states of H_2O^+

Dominique Dehareng

Département de Chimie, Université de Liège, Sart-Tilman, B 4000 Liége 1, Belgium

Xavier Chapuisat

Laboratoire de Chimie Théorique (CNRS-ERA 549), Bât. 490, Université de Paris-Sud, F-91405 Orsay Cédex, France

Jean-Claude Lorquet, Claudine Galloy, and Gheorghe Raseev

Département de Chimie, Université de Liège, Sart-Tilman, B 4000 Liège 1, Belgium
(Received 28 July 1981; accepted 24 September 1982)

The conical intersection connecting the $\tilde{B}\,^2A'$ and $\tilde{A}\,^2A'$ states of the H_2O^+ ion is studied. The two potential energy surfaces are calculated *ab initio* by the SCF/CI method within the C_s point group. The nonadiabatic coupling matrix elements $\langle\tilde{A}|\partial/\partial q|\tilde{B}\rangle$ are computed for several cross sections throughout the potential energy surfaces. A transformation to the diabatic representation is performed. The linear model is found to be a good approximation in the region close to the apex of the cone. The global functions *t(s)* and *T(S)* governing the nonadiabatic transition probability are calculated; their shapes are those predicted by the Landau–Zener model (in the Nikitin bidimensional version). A dynamical study is undertaken by means of classical trajectory calculations on the upper adiabatic potential energy surface. An averaged transition probability $\bar{P}_{tr}$ is derived. Excitation of rotation or of the bending mode of H_2O before photon impact has no influence on $\bar{P}_{tr}$. Excitation of the symmetrical or antisymmetrical valence modes of H_2O lowers $\bar{P}_{tr}$. The shape of $\ln(1-\bar{P}_{tr})$ as a function of time indicates the existence of two distinct regimes at short and intermediate time ranges, characterized by two different rate constants k_1 and k_2, respectively. The rate constants are of the order of $10^{14}\ s^{-1}$. k_1 exhibits a maximum as a function of the absorbed energy E_{abs}, whereas k_2 decreases as a function of E_{abs}.

I. INTRODUCTION

Classical trajectory calculations constitute a powerful tool for studies in chemical dynamics.[1,2] Most of the effort to date has dealt with adiabatic processes, i.e., situations where the Born–Oppenheimer approximation is valid everywhere, so that the problem is reduced to studying classical nuclear trajectories on a single potential energy surface. Such calculations have provided a direct illustration of the difference which exists among the reactivities of diatomic and polyatomic molecules.

The problem is far more complicated when surface crossings are considered. Such nonadiabatic processes,[3] which involve transitions between two (or possibly more) neighboring potential energy surfaces are, however, of common occurrence both in uni- and bimolecular reactions. Low-energy nonadiabatic collisions have been studied[4] by Tully and reviewed[5] by him. Nonadiabatic unimolecular processes[6–11] have received so far much less attention. In both cases, the solution requires the following steps:

(i) Calculation of two (or more) potential energy surfaces, preferably by means of *ab initio* configuration interaction (CI) methods;

(ii) Calculation of the off-diagonal (nonadiabatic) coupling matrix elements which bring about transitions between electronic states;

(iii) Calculation of a suitable set of nuclear trajectories;

(iv) Calculation of the nonadiabatic transition probability for each trajectory, either by numerical integration of the classical-trajectory equations (*vide infra*) or by some suitable closed-form formula;

(v) Calculation of a microcanonical rate constant by Monte Carlo averaging of the previous results as a function of the total energy.

The calculations can be done in either of the two available kinds of representations—adiabatic or diabatic.[12,13]

As an example, we have chosen to study the conical intersection which exists between the $\tilde{B}\,^2B_2$ and $\tilde{A}\,^2A_1$ states of the H_2O^+ ion, and which plays an essential role in the unimolecular dissociation of H_2O^+. This crossing has already a long story. In 1966, Fiquet-Fayard and Guyon[14] interpreted the fragmentation of the water ion as predissociations of the $\tilde{B}\,^2B_2$ state by two repulsive states—a quartet state for OH^+ production and a doublet state for H^+ formation. *Ab initio* calculation of the potential energy surfaces at the SCF level,[15] followed by a crude application of Fermi's Golden Rule,[16] demonstrated the plausibility of the model. Shortly afterwards, Eland was able to study the behavior of energy-selected ions by the photoion–photoelectron coincidence technique.[17] He suggested that the presence of strong vibronic interaction between states $\tilde{A}$ and $\tilde{B}$ could lead to a radiationless transition and could play an important role in the dissociation mechanism. Thus, according to Eland's interpretation, one has

 0021-9606/83/031246-19$2.10

$$H_2O(\tilde{X}\ ^1A_1) + h\nu \rightarrow H_2O^*(\tilde{B}\ ^2B_2/^2A') \rightarrow H_2O^*(\tilde{A}\ ^2A_1/^2A') \begin{matrix} \nearrow OH^* + H \\ \searrow H^* + OH \end{matrix}, \quad (1.1)$$

where the photon energy $h\nu$ ranges between 18.0 and 20.2 eV.

A number of potential energy surface calculations then appeared.[9,18-22] The valence-bond calculation of Balint-Kurti and Yardley[18] demonstrated the presence of a conical intersection between states $\tilde{A}$ and $\tilde{B}$. This was confirmed at the CI *ab initio* level, first by some of us,[9] then quite recently by Jackels[22] with a large-scale calculation.

The purpose of this paper is to present a detailed study of the nonadiabatic coupling around the conical intersection and particularly to examine its consequences on the dynamics of reaction (1.1).

The paper is organized as follows. In Sec. II, we briefly describe our CI calculations and find them to agree essentially with those calculated by Balint-Kurti[18] and by Jackels.[22] In Sec. III, we examine the region of strong nonadiabatic interaction around the apex of the double cone, and calculate *ab initio* the coupling matrix elements. In Sec. IV, we transform our *ab initio* results into the diabatic representation and compare them to the linear model.[11] In Sec. V, we calculate the global functions $t(s)$[23] and $T(S)$[10,11] and show the nonadiabatic transition probability to be correctly accounted for by Nikitin's bidimensional version of the Landau-Zener model.[3] The theoretical background of an overall three-dimensional dynamical study (by means of classical trajectories plus quantum-mechanical evaluation of the transition probability) of the passing through the conical intersection connecting states $\tilde{B}$ and $\tilde{A}$ is presented in Sec. VI. The numerical results are given in Sec. VII and discussed in order to investigate the dyn mics of the dissociation process suggested by Eland.

II. POTENTIAL ENERGY SURFACES

Since the calculation of the potential energy surfaces is only a first step in our study, it was decided, in order to keep the computational effort within reasonable limits, to look for the best compromise between simplicity of the wave function and accuracy in the description of the problem. Our AO basis set consisted in a Huzinaga[24] $(9s\ 5p \mid 4s)$ basis set with Dunning's $[3s\ 2p \mid 2s]$ contraction.[25] The influence of the AO basis set was checked, however. Inclusion of Rydberg diffuse AO's had virtually no effect on the position of the crossing, whereas inclusion of $3d_0$ and $2p_H$ polarization functions changed the angle of crossing from 71.6° to 75.4° (i.e., close to the value calculated by Jackels[22]), but otherwise had no influence on the shape of the nonadiabatic coupling function (to be defined in Sec. III).

Cumbersome nonorthogonality problems in the calculation of the off-diagonal matrix elements were avoided by calculating the wave functions of the $\tilde{A}$ and $\tilde{B}$ states (which belong to the same $^2A'$ representation in the C_s point group) as two roots of the same CI matrix in the C_s point group. This procedure requires an expansion in the same basis set of molecular orbitals. To avoid any known bias in the relative accuracy of the two states, we adopted the MO's of the closed shell ground state of neutral H_2O represented by configuration Φ_1:

$$\tilde{X}\ ^1A_1/^1A' : (1a_1/1a')^2(2a_1/2a')^2(1b_2/3a')^2 \times (3a_1/4a')^2(1b_1/1a'')^2 . \quad (\Phi_1)$$

Comparing configuration Φ_1 with the leading terms in the CI expansion of states $\tilde{A}$ and $\tilde{B}$ of the ion (configurations Φ_2 and Φ_3, respectively)

$$\tilde{A}\ ^2A_1/^2A' : (1a_1/1a')^2(2a_1/2a')^2(1b_2/3a')^2 \times (3a_1/4a')^1(1b_1/1a'')^2 , \quad (\Phi_2)$$

$$\tilde{B}\ ^2B_2/^2A' : (1a_1/1a')^2(2a_1/2a')^2(1b_2/3a')^1 \times (3a_1/4a')^2(1b_1/1a'')^2 , \quad (\Phi_3)$$

one sees that configurations Φ_2 and Φ_3 differ from Φ_1 by the occupation number of $3a_1$ and $1b_2$, respectively. Therefore, adopting the MO's of configuration Φ_1 to describe states $\tilde{A}$ and $\tilde{B}$ amounts to adopting the intermediate configuration (also termed the intermediate Hamiltonian) technique.[26]

The CI expansion was truncated after inclusion of all monoexcited configurations of Φ_2 and Φ_3. This generated 69 CSF's. As a check, a cross section of the potential energy surfaces was also calculated with the inclusion of all doubly excited configurations. This extended the size of the CI matrix to 568 CSF's but had no influence on the position of the crossing and on the shape of the coupling function.

All the calculations were performed with the MOLALCH system of programs.[27]

Throughout the paper, the nuclear positions will be described by a set of three internal symmetry coordinates R, r, and α, where

$$R = \tfrac{1}{2}(R_1 + R_2) , \quad r = (R_1 - R_2) , \quad (2.1)$$

R_1 and R_2 being the two OH bond lengths (see Fig. 1) and α the valence angle.

When the two OH bond lengths are equal ($r = 0$; C_{2v} point group), states $\tilde{A}$ and $\tilde{B}$ belong to the $^2A_1$ and $^2B_2$ representations, respectively. Their potential energy curves cross. When the antisymmetrical stretching coordinate r is different from zero, i.e., when the two OH bond lengths are unequal, these two states both belong to the $^2A'$ representation of the C_s point group and avoid crossing. A schematic view is given in Fig. 2, where the potential energy surfaces are plotted as a function of the internuclear valence angle α and the antisymmetric stretching coordinate r. As a result, a region of strong nonadiabatic interaction is centered around the apex of the double cone.

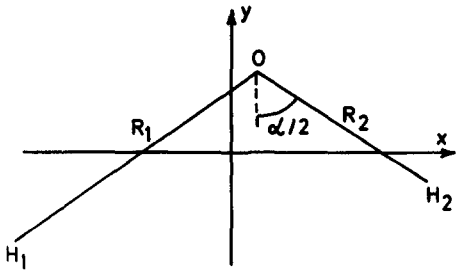

FIG. 1. Definition of the internal coordinates R_1, R_2, and α in the body fixed frame.

It was also noticed that the two interacting states $\tilde{A}$ and $\tilde{B}$ are well separated in energy from the remaining ones. In other words, one is dealing here with a two-state conical intersection problem. In the terminology of our previous paper,[11] r is the symmetry-lowering coordinate y, whereas R and α qualify equally well as the symmetry-conserving coordinate x (see below).

A total number of 250 *ab initio* calculations was performed to generate graphically a three-dimensional grid of points. Energy contour plots are represented in Figs. 3–6. In particular, it appears (Figs. 5 and 6) that the position of the apex of the double cone is a function of the two totally symmetrical coordinates R and α. In the subspace $r = 0$, this locus coincides with the "seam"[4,5,8(a)] between diabatic surfaces.

III. COUPLING IN ADIABATIC REPRESENTATION

The semiclassical approximation[3–5,9–12] is especially convenient for a description of the nonadiabatic coupling which results from the breakdown of the Born-Oppenheimer approximation in the vicinity of the apex of the cone. In this approximation, the nuclear motion is described by a classical trajectory, whereas the electronic coordinates are treated quantum mechanically. Since the *ab initio* calculations reported in the previous section indicate that the problem under study can be described as an interaction between two electronic states only, the electronic wave function can be expanded in two terms:

$$\psi^{el}(\tau) = \sum_{k=1}^{2} a_k(\tau)\,\eta_k \exp\left[-(i/\hbar)\int_0^{\tau} H_{kk}\,d\tau\right] \qquad (3.1)$$

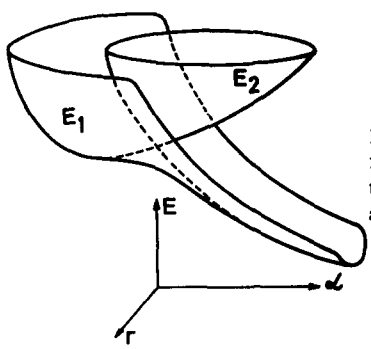

FIG. 2. Perspective drawing of the $\tilde{B}\,^2B_2$ and $\tilde{A}^2A_1$ potential energy surfaces in the adiabatic representation.

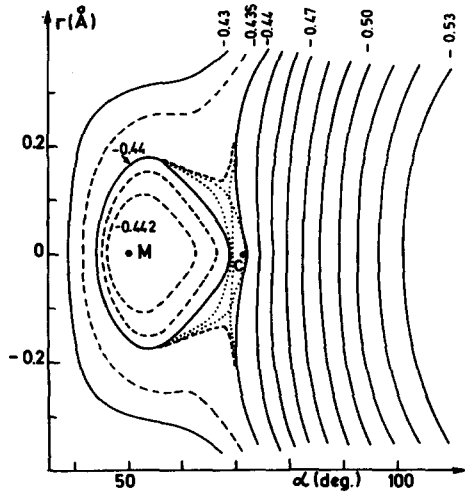

FIG. 3. Potential energy surface of the lower adiabatic surface E_1 as a function of coordinates r and α, with $R = 1.15$ Å. The contour interval is 0.01 a.u. Additional contours have been drawn in dashed and dotted lines. Dashed lines—additional contours at −75.435, −75.439, −75.441, and −75.442 hartree. Dotted lines—additional contours at −75.4393 and −75.4395 hartree. The reported energies are the absolute energies to which a constant value of +75 hartrees have been added. Point C is the apex of the cone (at an energy equal to −75.4385 hartree.). Point M is the energy minimum of the $\tilde{B}\,^2B_2$ state and lies at an energy of −75.4435 hartree.

where τ is the time, H is the electronic Hamiltonian, a_1 and a_2 are expansion coefficients in a certain basis set of electronic functions η_1 and η_2. Two such basis sets are especially convenient. One of them is dis-

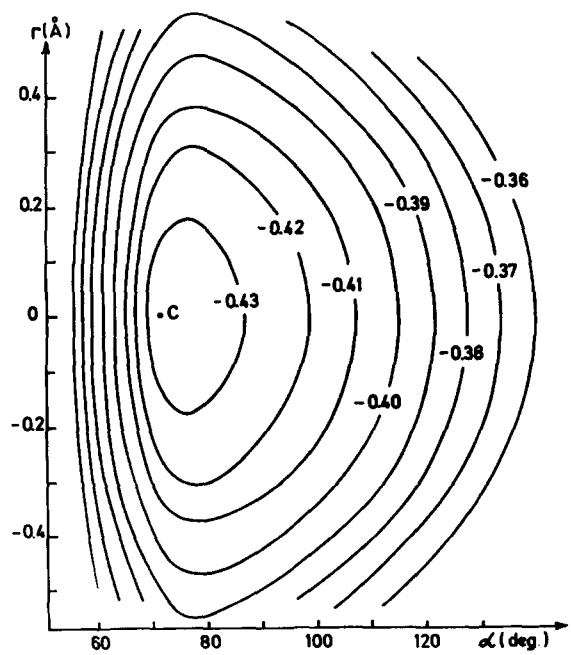

FIG. 4. Potential energy surface of the upper adiabatic surface E_2 as a function of coordinates r and α, with $R = 1.15$ Å. The contour interval is 0.01 hartree. Point C is the apex of the cone and lies at an energy of −75.4385 hartree. This is the potential with which all the trajectory calculations have been done. The reported energies are the absolute energies to which a constant value of +75 hartrees has been added.

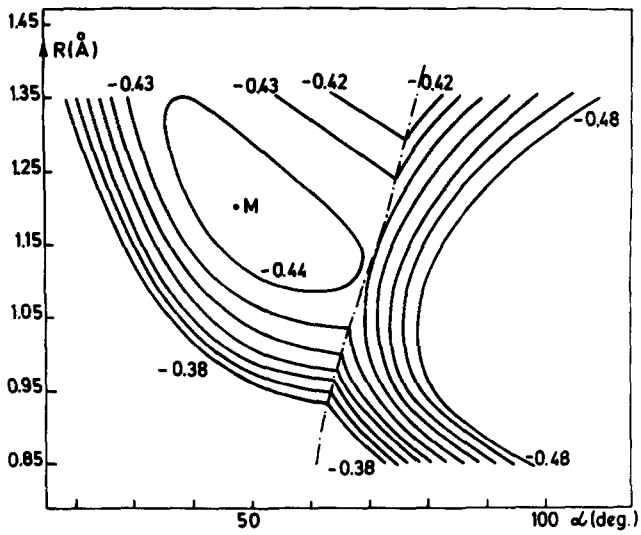

FIG. 5. Lower adiabatic energy surface E_1 as a function of coordinates R and α, for $\tau = 0$. The contour interval is 0.01 hartree. The reported energies are the absolute energies of the CI calculation to which a constant quantity of +75 hartrees has been added. Point M is the energy minimum of the $\tilde{B}\,^2B_2$ state and lies at an energy of -75.4456 hartrees. The discontinuous nature of this surface is clearly exhibited on this picture and the locus of the discontinuity (which corresponds to the apex of the cone or to the seam between the diabatic surfaces) is represented with a dash–dot line.

cussed below. The other will be considered in Sec. IV.

The most straightforward choice consists in adopting the set of eigenfunctions $|k\rangle$ of the electronic Hamiltonian H:

$$H|k\rangle = E_k|k\rangle\,, \quad k = 1,\ 2\,. \tag{3.2}$$

This choice gives rise to the so-called adiabatic representation. The nonadiabatic coupling is then due to the off-diagonal matrix elements of the $\partial/\partial q_j$ operators:

$$g_j = \langle 2|\,\partial/\partial q_j\,|1\rangle\,. \tag{3.3}$$

In a polyatomic molecule, these quantities can be considered as the elements of a $(3N-6)$-dimensional coupling vector $\mathbf{g}$.[11]

The expansion coefficients are solution of a system of coupled differential equations (the so-called classical-trajectory equations)[3–5,10–12]:

$$\begin{aligned}\dot{a}_1 &= a_2\,\mathbf{g}\cdot\dot{\mathbf{q}}\exp\left[-(i/\hbar)\int^{\tau}\Delta E\,d\tau\right]\,,\\ \dot{a}_2 &= -a_1\,\mathbf{g}\cdot\dot{\mathbf{q}}\exp\left[(i/\hbar)\int^{\tau}\Delta E\,d\tau\right]\,.\end{aligned} \tag{3.4}$$

A nonadiabatic coupling matrix element g_j can be calculated by numerical differentiation of the LCAO and CI coefficients as described in Refs. 8 and 11. Let the CI expansion of the two adiabatic states by represented by

$$|1\rangle = \sum_m A_m\Phi_m\,, \quad |2\rangle = \sum_n B_n\Phi_n\,, \tag{3.5}$$

where the Φ's are linear combinations of Slater determinants chosen to be eigenfunctions of spin and symmetry and called configuration state functions (CSF). The coupling matrix element g is split into two contributions:

$$\begin{aligned}g &= \langle 2|\,\partial/\partial q\,|1\rangle = \sum_m (\partial A_m/\partial q)B_m + \sum_{\substack{m\\ m\neq n}}\sum_n A_mB_n\langle\Phi_n|\,\partial/\partial q\,|\Phi_m\rangle\\ &\equiv g^{\mathrm{CI}} + g^{\mathrm{MO}}\,.\end{aligned} \tag{3.6}$$

g^{CI} results from the derivative of the CI coefficients. It is calculated by differentiating a five-point Lagrange polynomial fitted to the CI coefficients. As a check, we also used spline differentiation.[1(b),28] The two methods were found to practically give the same result. The accuracy is estimated to be better than three (and in most cases four) significant digits.

The second term appearing in Eq. (3.6) includes matrix elements $\langle\Phi_m|\,\partial/\partial q\,|\Phi_n\rangle$ where Φ_m and Φ_n are CSF's. They are reduced to the form $\langle\phi_i|\,\partial/\partial q\,|\phi_j\rangle$ where ϕ_i and ϕ_j are MO's by means of a transition matrix formalism:

$$\begin{aligned}g^{\mathrm{MO}} &= \sum_{\substack{m\\ m\neq n}}\sum_n A_mB_n\langle\Phi_m|\,\partial/\partial q\,|\Phi_n\rangle\\ &= \sum_{\substack{i\\ i\neq j}}\sum_j T_{ij}\langle\phi_i|\,\partial/\partial q\,|\phi_j\rangle\,.\end{aligned} \tag{3.7}$$

T_{ij} is an element of the so-called first-order transition matrix.[29] For a given pair of CSF's Φ_m and Φ_n, the matrix which gives the contribution of the different Slater determinants which make up Φ_m and Φ_n can be extracted from the list of symbolic energy matrix elements which calculated once for all in the MOLALCH system of programs.[30] The matrix elements $\langle\phi_i|\,\partial/\partial q\,|\phi_j\rangle$ are calculated by the "double molecule" method.[8,11] A finite difference approximation is used for the derivative; this leads to the calculation of a differential AO overlap matrix. There is an optimum value for the finite dif-

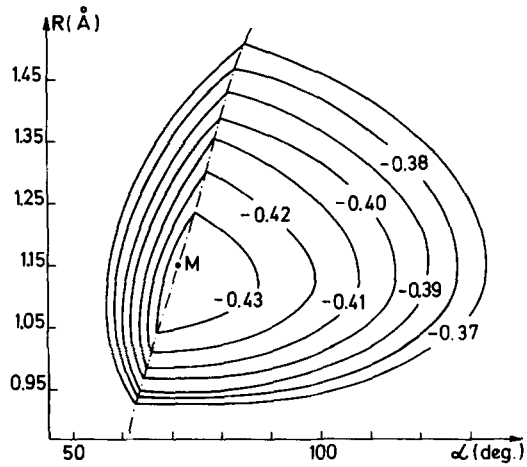

FIG. 6. Upper adiabatic energy surface E_2 as a function of coordinates R and α for $\tau = 0$. The contour interval is 0.01 hartree. The reported energies are the absolute energies of the CI calculation to which a constant value of +75 hartrees has been added. Point M is the energy minimum (energy = -75.4385 hartrees).

ference Δq which gives rise to a compromise between the accuracy of the derivative and the rounding-off errors due to the finite computer word size. The following values were chosen: $\Delta\alpha = 0.06°$ and $\Delta r = 10^{-4}$ Å. The results are then accurate to four or five significant digits

The transition matrix formalism offers two advantages. Firstly, it considerably speeds up the calculation of g^{MO}, especially for large CI matrices. Secondly, inspection of the transition matrix T_{ij} allows one to immediately detect the particular MO's which provide the largest contribution to g^{MO}. Large contributions were found to result from avoided crossings between molecular orbitals. This is readily understood if the matrix element is expressed in terms of orbital energies ϵ_i and ϵ_j of a closed-shell structure. Then, one has approximately

$$\langle \phi_i \,|\, \partial/\partial q \,|\, \phi_j \rangle = (\epsilon_j - \epsilon_i)^{-1} \langle \phi_i \,|\, \partial H^{scf}/\partial q \,|\, \phi_j \rangle \qquad (3.8)$$

(this result is strictly true when the basis is complete).

In the case of H_2O^+, when R is equal to 1.15 Å, such an avoided crossing between the $(1b_2/3a')$ and $(3a_1/4a')$ MO's takes place at $\alpha = 77.5°$, whereas the crossing between electronic surfaces takes place at $\alpha = 71.6°$ (Fig. 7). As a result, g^{MO} exhibits a spurious extremum at the orbital crossing which, however, is partly cancelled by an extremum of opposite sign of g^{CI}. The

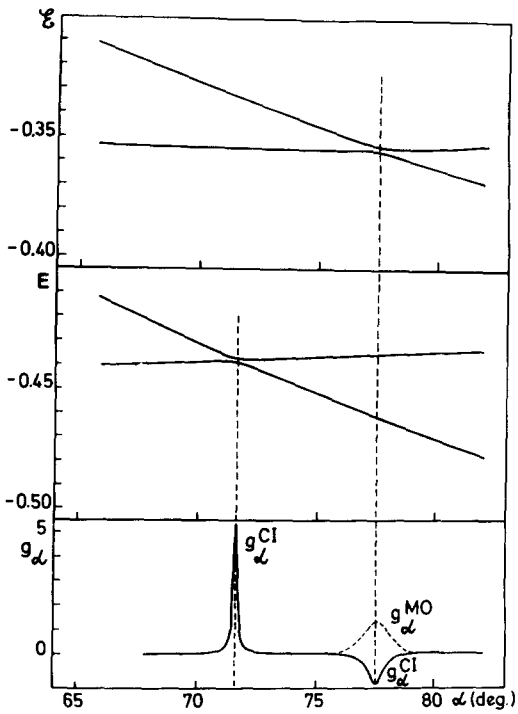

FIG. 7. Upper part: Energies $\mathcal{E}_i$ of two Slater determinants corresponding to configurations Φ_2 and Φ_3 (before CI diagonalization) as a function of valence angle α for $R = 1.15$ and $r = 0.005$ Å, showing an avoided crossing at $\alpha = 77.5°$. Middle part: Adiabatic energies E_i (after CI diagonalization) for the same set of coordinates showing an avoided crossing at $\alpha = 71.6°$. A constant value of +75 hartrees has been added to the energies. Lower part: Nonadiabatic coupling matrix element g_α for $r = 0.005$ Å and $R = 1.15$ Å, showing the partial cancellation of its two contributions—g_α^{CI} (solid line) and g_α^{MO} (broken line).

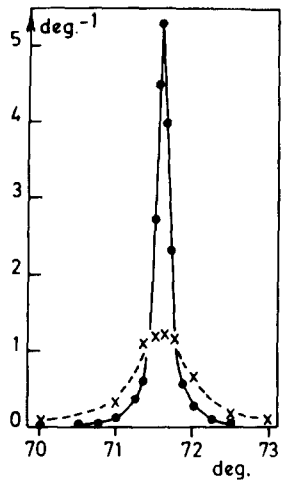

FIG. 8. Total nonadiabatic coupling matrix element g_α for two different cross sections at $R = 1.15$ Å. Black dots: numerical values of g_α for $r = 0.005$ Å; the solid line is a Lorentzian fitted to them. Crosses: numerical values of g_α for $r = 0.02$ Å; the dashed line is a Lorentzian fit to them.

resulting total function g_α has a Lorentzian shape with a unique maximum centered at the crossing between the two surfaces, as it should (Fig. 8).

Five such functions g_α were calculated at $r = 0.005$, 0.02, 0.04, 0.1, and 0.2 Å (although, for the sake of brevity, only two of them are reported in Figs. 7 and 8). Along the other direction, five functions g_r were calculated at $\alpha = 65°$, 70°, 71.5°, 74°, and 77°.

Along direction r, both g_r^{CI} and g_r^{MO} are symmetric with respect to $r = 0$. Their sum g_r has again a unique maximum and a Lorentzian shape, although the two contributions sometimes add and sometimes subtract. g_r is found to be positive at values of α smaller than α_c and negative for α larger than α_c (Fig. 9), where α_c denotes the value of the valence angle at the apex of the cone.

The closer the cross section to the apex of the cone, the narrower the g function. In the case where the cross section goes through the apex of the cone, the linear model predicts (Ref. 11 and Sec. IV B below)

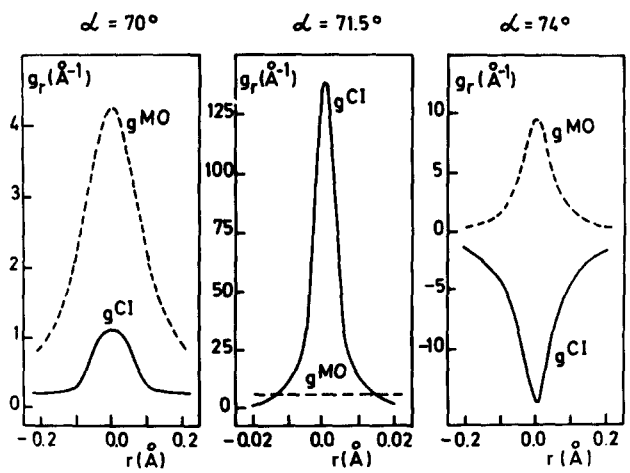

FIG. 9. The two components of the nonadiabatic coupling matrix element g_r^{CI} and g_r^{MO} as a function of r for different values of α. Left frame: $\alpha = 70°$. Middle frame: $\alpha = 71.5°$. Right frame: $\alpha = 74°$.

that the g function should become a Dirac delta function. For $R = 1.15$ Å

$$\lim_{r\to 0}\langle 2|\partial/\partial\alpha|1\rangle = \delta(\alpha - 71.6^\circ)\frac{\pi}{2}, \tag{3.9}$$

$$\lim_{\alpha\to 71.6^\circ}\langle 2|\partial/\partial r|1\rangle = \delta(r)\frac{\pi}{2}. \tag{3.10}$$

A comparison between Figs. 8 and 9 shows that it is seemingly the case.

These results will be discussed in more detail within the framework of the linear model (Sec. IV). Nevertheless, we already note that the g_j functions which we calculate have an area

$$A_j \equiv \int_{q_j^{\min}}^{q_j^{\max}} g_j(q_j)\,dq_j, \tag{3.11}$$

which is very close to the theoretical value of $\pi/2$ [8,10,11] (the integral is taken over the entire space where g is different from zero). The deviations (9% in the most unfavorable case) give an indication of the accuracy of our coupling matrix elements.

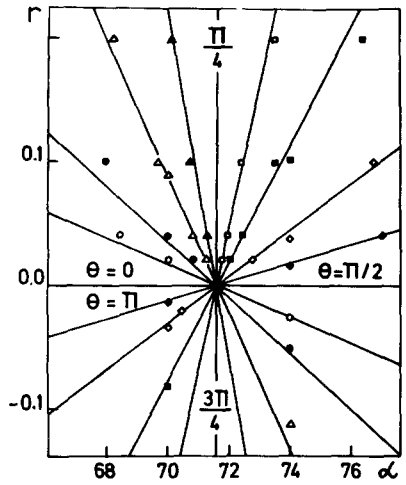

FIG. 10. Locus of points where θ = constant. Each particular value of θ (module $\pi/2$) is represented by a different symbol ($\theta = 0.1$: open circles; $\theta = 0.2$: filled circles; $\theta = 0.4$: open triangles; $\theta = 0.6$: filled triangles; $\theta = 1$: open squares; $\theta = 1.2$: filled squares; $\theta = 1.4$: open diamonds; $\theta = 1.5$: filled diamonds). Coordinate R is fixed at $R = 1.15$ Å.

IV. COUPLING IN DIABATIC REPRESENTATION

A. Diabatic states

In the diabatic representation, the electronic Hamiltonian H is no longer diagonal. The potential energy surfaces are defined as the diagonal elements H_{11} and H_{22}. They can cross freely and are coupled by an off-diagonal matrix element H_{12}. In the semiclassical approximation, the diabatic basis is defined as the basis that diagonalizes the vectorial operator

$$\nabla = \left\{\frac{\partial}{\partial q_1}, \ldots, \frac{\partial}{\partial q_{3N-6}}\right\},$$

(Ref. 11). In the quantum mechanical formalism,[48–50] the diabatic basis is defined as the basis for which all the couplings are of potential nature. Such a basis can be derived from the adiabatic one only under certain conditions[13,48–50] involving a relationship between the coupling matrix elements. If these conditions are fulfilled, the transformation matrix exists and is orthogonal. In the two-state approximation under study, this is very nearly the case[51]. One has then

$$\begin{pmatrix}|1\rangle\\ |2\rangle\end{pmatrix} = \begin{pmatrix}\cos\theta & \sin\theta\\ -\sin\theta & \cos\theta\end{pmatrix}\begin{pmatrix}\chi_1\\ \chi_2\end{pmatrix}, \tag{4.1}$$

where

$$\theta = (1/2)\arctan[2H_{12}/(H_{11} - H_{22})]. \tag{4.2}$$

Furthermore, one has[11]

$$g_j = \partial\theta/\partial q_j \tag{4.3}$$

The numerical procedure to integrate Eq. (4.3) and define the diabatic states is not arbitrary. For example, in the two-dimensional (let us say r and α) case the solution must verify the relationship

$$\theta = \int_{r_0}^{r} dr\, g_r(r,\alpha) + \int_{\alpha_0}^{\alpha} d\alpha\, g_\alpha(r_0,\alpha), \quad \text{(Ref. 48)}.$$

In the present case, this can be ensured as follows: Eq. (4.3), which defines an angle θ which is a function of the three internal coordinates R, r, and α, was numerically integrated for a fixed value of $R = 1.15$ Å (i.e., close to the equilibrium value of the $\tilde{B}$ state), thus reducing the problem to two dimensions, r and α. The integration grid consisted of 25 points, obtained from five points along direction α and five points along direction r (cf. Sec. III). The integration constant was determined by assigning to θ a value of zero along the negative part of the symmetry-conserving axis α, thus wherever $r = 0$ and $\alpha < 71.6°$. The solution was then propagated by numerical integration of the *ab initio* calculated g_j matrix elements. The value of θ at a particular point was in many cases checked to be independent of the integration path followed. The results are given in Fig. 10. One checks that a complete loop around the apex of the cone increases θ by a value of π. In other words, θ is a multivalued function defined (as usual) modulo π. This does not alter the orthogonal transformation relating diabatic and adiabatic states.

The multivaluation of the function is due to the fact that the functions g_α and g_r present a singularity at ($\alpha = 71.6°$, $r = 0$ Å). As a consequence, the value of θ at the point (α, r) depends on the path selected to connect the point (α, r) to the point (α_0, r_0) in the path integral giving θ.[52,53]

Once θ is known as a function of the internal coordinates, it is not difficult to obtain the diabatic energies H_{11} and H_{22} and the coupling matrix element H_{12} by inverting the orthogonal transformation (4.1).[11] The corresponding diabatic representation is hereafter called the "canonical diabatic representation." A schematic view of the diabatic surfaces H_{11} and H_{22} is given in Fig. 11. The numerical errors inherent in the calculation of the g functions are of little influence on the values of H_{11} and H_{22}, but more deeply affect the value of H_{12}.

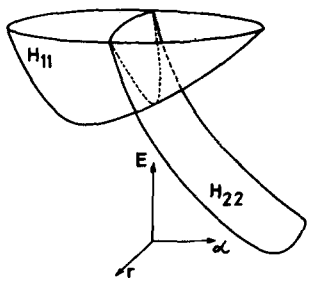

FIG. 11. Perspective drawing of the $\tilde{B}$ and $\tilde{A}$ states in the diabatic representation. The seem is represented by a dotted line.

B. The linear model

The linear model of a conical intersection[3,11] amounts to neglecting higher-order terms in the Maclaurin expansion of the diabatic quantities around the apex of the cone

$$H_{11} - H_{22} = F_\alpha(\alpha - \alpha_c) \ , \tag{4.4}$$

$$H_{12} = (1/2)\, F_r\, r \ . \tag{4.5}$$

It should be kept in mind that α_c is a function of R.

As a consequence, one has[11]

$$\theta(\alpha, r) = (1/2)\arctan[F_r r/F_\alpha(\alpha - \alpha_c)] \ , \tag{4.6}$$

$$g_\alpha(\alpha) = \left(\frac{\partial\theta}{\partial\alpha}\right)_{R,r} = \frac{-F_\alpha/(2F_r r)}{1 + (F_\alpha/F_r r)^2(\alpha - \alpha_c)^2} \ ,$$

$$g_r(r) = \left(\frac{\partial\theta}{\partial r}\right)_{R,\alpha} = \frac{F_r/[2F_\alpha(\alpha - \alpha_c)]}{1 + [F_r/F_\alpha(\alpha - \alpha_c)]^2 r^2} \ . \tag{4.7}$$

Thus, for a given value of r, g_α is a Lorentzian function of α centered at α_c, and conversely for the other case.

Equations (4.6) and (4.7) were used to check the validity of the linear model by comparison with numerical calculations reported in Sec. IV A for a value of R equal to 1.15 Å (i.e., close to the equilibrium value of the $\tilde{B}$ state). Equation (4.6) predicts a series of straight lines around the apex of the cone for the locus of constant θ. This is borne out by the calculations (Fig. 10). In particular, the seam between diabatic states (i.e., their line of intersection) corresponds to the locus $H_{11} = H_{22}$, or $\theta = (\pi/4) + (k\pi/2)$. To a very good approximation, it is found to coincide with axis r at $\alpha = 71.6°$.

According to Eqs. (4.7), the closer the cross section to the apex of the cone, the sharper the resulting Lorentzian. Figures 8 and 9 show that this is qualitatively the case. Quantitatively, a better fit was obtained for g_α than for g_r. This indicates that the diabatic surfaces are locally planes in the immediate neighborhood of the apex of the cone, as predicted by Eq. (4.4), but exhibit some curvature further away (Fig. 11).

Using the linear model minimizes the effort, since the situation can be described by two parameters only: F_α and F_r. F_α can be read directly on a cross section along axis α at $r = 0$, since the diabatic and adiabatic surfaces then coincide. The result is $F_\alpha = 4.5\ 10^{-3}$ hartree/deg. A value of $4.2\ 10^{-3}$ hartree/deg was obtained by Jackels.[22] F_r can be determined[11] from the shape of the adiabatic curves along axis r, via Eqs. (4.5) and (4.8),

$$\Delta E = -2H_{12}/\sin 2\theta \ , \tag{4.8}$$

where ΔE is the energy difference between the adiabatic curves. One finds $F_r = 0.045$ hartree/bohr, compared to a value of 0.054 obtained by Jackels.

It was thus decided to assume the validity of the linear model for all values of R. F_α and F_r are determined as described in the previous paragraph. They are then functions of R. Numerical values are reported in Table I.

TABLE I. Numerical values of α_c (degrees), F_α (hartree/degree) and F_r (hartree/Å) for several values of R(Å).

R	α_c	F_α	F_r
0.90	61.5	0.005 47	0.12
0.95	63.5	0.005 47	0.20
1.05	67.5	0.004 85	0.25
1.15	71.6	0.004 50	0.09
1.25	75.0	0.004 20	0.08
1.35	78.5	0.003 70	0.07
1.40	79.5	0.003 38	
1.45	81.2	0.003 20	
1.60	86.0	0.002 93	
1.90	95.5	0.002 72	0.04

V. NONADIABATIC TRANSITION PROBABILITIES

The semiclassical calculation of transition probabilities through a conical intersection involves two steps:

(i) transformation of the canonical diabatic representation into the Nikitin diabatic representation[3,11];

(ii) selection of an appropriate model on the basis of the shape of the global functions $t(s)$ and $T(S)$.[10,11,23]

Let us characterize a linear trajectory by its slope γ and by l, the nearest approach distance to the apex of the cone (Fig. 12). Let $\dot{\alpha}$ and $\dot{r}$ be the nuclear velocities along axes α and r, respectively. Along such a trajectory, the angle θ varies from an initial value $\theta_{-\infty}$ to a final value $\theta_{+\infty}$. Then, $|\theta_{+\infty} - \theta_{-\infty}| = \pi/2$. Nikitin defines[3,11] for each trajectory an additional diabatic basis $(\bar{\chi}_1, \bar{\chi}_2)$ calculated by applying a constant unitary transformation to the canonical diabatic basis (χ_1, χ_2) defined by Eqs. (4.1). $(\bar{\chi}_1, \bar{\chi}_2)$ are then related to the adiabatic basis $(|1\rangle, |2\rangle)$ by an angle $\bar{\theta} = \theta + \bar{\phi}$, with $\bar{\phi}$ chosen so that $\theta_{-\infty} = 0$. Then, automatically, $\theta_{+\infty} = \pi/2$ and we are brought back to the diatomic case.

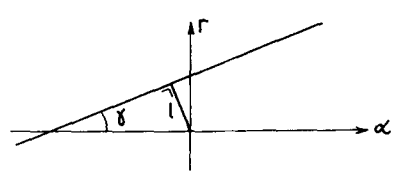

FIG. 12. Definition of the parameters γ and l for a linear trajectory in two dimensions.

In order to determine the most appropriate one-dimensional model for the calculation of the transition probability, the global functions[10,11] of the trajectory must be calculated. This concept was introduced by Delos and Thorson[23] who showed that in the semiclassical approximation, a curve crossing problem was completely characterized in the diabatic representation by a single function hereafter called the Delos–Thorson function $t(s)$. This means that the transition probability does not depend upon the detailed properties of the four diabatic quantities H_{11}, H_{22}, H_{12}, and $\dot{q}$ considered separately, but only on a global function of them $t(s)$ or $t(s-s_c)$ where

$$t = -\cot 2\theta \ , \tag{5.1}$$

$$s = \int_0^\tau (H_{12}/\hbar)\, d\tau' \ , \tag{5.2}$$

and s_c is the value of s at the crossing point.[31] Each model (Landau–Zener, Rosen–Zener, Delos–Thorson, Nikitin, or Bandrauk) is completely characterized by its own function $t(s)$.[10] In other words, a particular crossing may correspond, e.g., to the LZ model, even if the specific conditions which define the LZ model (H_{11} and H_{22} linear, H_{12} and $\dot{q}$ constant) are not fulfilled. The only condition[10,23] is that t should be a linear function of s

$$t^{LZ}(s-s_c) = (4/\xi)\,(s-s_c) \ , \tag{5.3}$$

where ξ is the usual Massey parameter.[3,10]

A corresponding function $T(S)$, called the Massey function, also exists[10] in the adiabatic representation and has similar properties

$$T = \Delta E/\hbar\dot{\mathbf{q}}\cdot\mathbf{g} = \Delta E/\hbar\dot{\theta} \ , \tag{5.2}$$

$$S = \theta - \pi/4 \ . \tag{5.3}$$

The Massey function offers the advantage that it can be obtained in a straightforward way from the *ab initio* calculations reported in the previous sections. Once $T(S)$ has been calculated in the adiabatic representation, it is easy to derive the corresponding global function $t(s-s_c)$ in the diabatic representation. As already noted,[31] $t(s)$ and $T(S)$ are calculated for each particular cross section in the potential energy surface, and thus relate to the Nikitin diabatic representation. Subsequent transformation to the canonical diabatic representation is, however, possible. More details are given in Refs. 10 and 11. Results are given in Figs. 13–16.

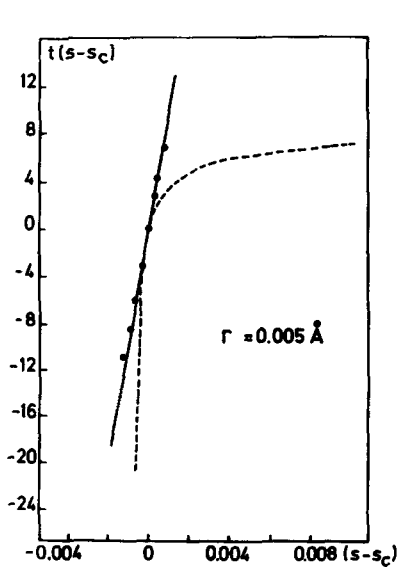

FIG. 13. Delos–Thorson function $t(s-s_c)$ for $r = 0.005$ Å and $R = 1.15$ Å. The full line is the function $(4/\xi)\,(s-s_c)$. The dashed line is obtained by calculating t and $(s-s_c)$ from numerical values of θ. The dots are derived by calculating t and $(s-s_c)$ from an analytical expression for θ.

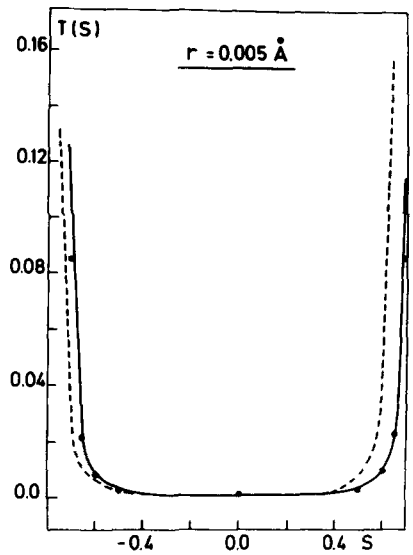

FIG. 14. Massey function $T(S)$ for $r = 0.005$ Å and $R = 1.15$ Å. The dots are the values obtained by the analytical expression $\xi/\cos^3(2s)$. The full line is obtained with a Lorentzian fit for g_α. The dashed line is obtained with numerical values of g_α.

Global functions depend on the nuclear velocity and thus on the total energy of the system, as shown in Figs. 15 and 16.[32] On the whole, Massey functions $T(S)$ are found to be well described by the function $\xi/\cos^3(2S)$ whereas Delos–Thorson functions $t(s)$ obey Eq. (5.3). This implies[10,11] that the LZ model is valid, and that transition probabilities can be calculated by means of the Nikitin formula

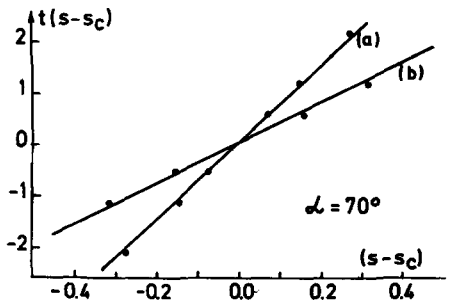

FIG. 15. Delos–Thorson function $t(s-s_c)$ for $\alpha = 70°$ and $R = 1.15$ Å., obtained for two different initial kinetic energies. The full lines represent the theoretical functions $(4/\xi)\,(s-s_c)$. The dots are obtained with numerical values for θ. Curve (a): E_{kin}^{in} ($r^{in} = 0.1$ Å) $\simeq 0.23$ eV ($\xi = 1.039$); Curve (b): E_{kin}^{in} ($r^{in} = 0.1$ Å) $\simeq 1.05$ eV ($\xi = 0.544$).

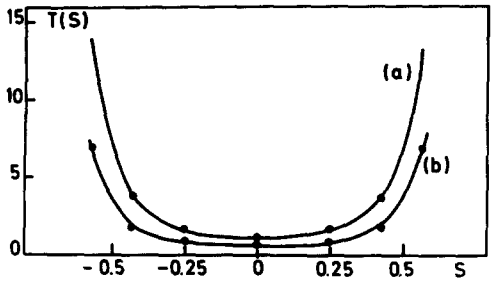

FIG. 16. Massey function $T(s)$ for $\alpha = 70°$ and $R = 1.15$ Å, obtained for two differential initial kinetic energies. The full lines represent the theoretical functions $\xi/\cos^3(2S)$. The dots are obtained with numerical values for g_r. Curve (a): $E_{\text{kin}}^{\text{in}}$ ($r^{\text{in}} = 0.1$ Å) $\simeq 0.23$ eV ($\xi = 1.039$); Curve (b): $E_{\text{kin}}^{\text{in}}$ ($r^{\text{in}} = 0.1$ Å) $\simeq 1.05$ eV ($\xi = 0.544$).

$$p = \exp\left\{ - \frac{\pi(F_\alpha \dot{\alpha} F_r \dot{r})^2 [(r/\dot{r}) - (\alpha - \alpha_c)/\dot{\alpha}]^2}{2\hbar(F_\alpha^2 \dot{\alpha}^2 + F_r^2 \dot{r}^2)^{3/2}} \right\} . \quad (5.4)$$

More details will be given in Sec. VI F.

The calculation of the global functions can be done either with numerical values of the g function, or with a Lorentzian fit to it. There are deviations with respect to the LZ model for large values of S and $s - s_c$ if numerical values of the g function are used. The deviations are slight for the Massey function, but are large for the Delos–Thorson function. This sensitivity can be understood as follows: The function t is equal to $-\cot(2\theta)$, and hence should tend towards a limit of $+\infty$ as $\theta \to \pi/2$. However, θ is obtained by numerical integration of a calculated g function, and its limit value may differ from the theoretical value of $\pi/2$ by a few percent. If, e.g., the area of the g function is equal to 87°, the t function will level off at a value of $-\cot(2 \times 87°) = 9.5$ instead of $+\infty$ (cf. Fig. 13).

VI. DYNAMICAL STUDY: THE MODEL

Some of the technical ingredients used in the dynamical study of the photodecomposition under consideration are summarized below. As many articles have appeared which review in detail the technical possibilities in the various aspects of the problem, we restrict ourselves to what is specific for the present treatment. For what is of a more standard use, only references will be given.

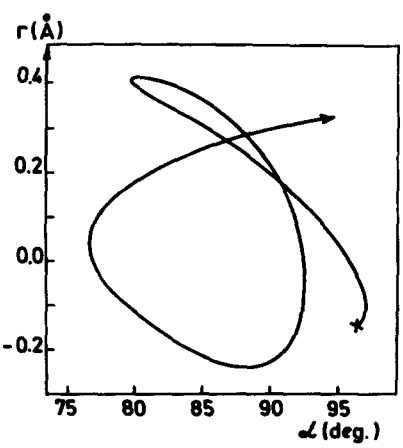

FIG. 17. Classical trajectory started from the cross ($\tau = 0$) and ended for $\tau = 1000$ a.u. of time, showing the variation of r(Å) vs α (deg) for $E_{\text{abs}} = 18.5$ eV, $J = 3$, $v_1 = v_2 = v_3 = 0$.

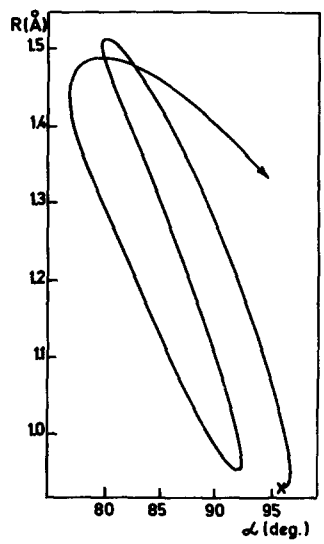

FIG. 18. Same classical trajectory as in Fig. 17, but showing the variation of R (Å) vs α(deg).

A. Interpolation of the potential energy function

To map the potential energy surfaces of the $\tilde{A}$ and $\tilde{B}$ states (Figs. 3–6), 180 points were computed in the range $\{\alpha\epsilon[50°, 120°]$, $r\epsilon[0°, 0.3$ Å$]$, $R\epsilon[0.85$ Å, 1.35 Å$]\}$. This is, however, insufficient for dynamical calculations, because, as a consequence of the centrifugal and whirlpool effects and of the strong coupling between all the modes of distortion of the molecular system, all the points of the upper adiabatic potential energy surface (whose topography is that of a cone) can be reached by the representative point of a trajectory after whirling a long time in the cone (see, e.g., Figs. 17 and 18). Additional points were therefore calculated in the range $\{\alpha\epsilon[50°, 140°]$, $r\epsilon[0, 1$ Å$]$, $R\epsilon[0.85$ Å, 1.9 Å$]\}$. Furthermore, locally interpolated values were added to the three-dimensional grid of the computed values of the potential. For the final results, 250 *ab initio* points were used for each state and 8778 points (for the upper adiabatic surface only) were used in the grid.

Various formulas were tested to analytically interpolate the potential energy function of the $\tilde{B}$ state, either in diabatic or in adiabatic representation. None of them was satisfactory everywhere. Thus, we turned to the technique of the three-dimensional cubic spline fitting.[1(b),28] The analytical method and the program used are due to Leforestier; they work within the context of the intrinsic spline interpolation. The basic ideas are:

(i) the values of the function which has to be interpolated—and they only—are given at the mesh points of the three-dimensional grid;

(ii) the partial derivatives on the boundaries of the grid—that are necessary to completely specify the spline function—are estimated by local interpolation (four point

TABLE II. Transition probability values for the onwards and backwards trajectories, obtained by the AM and BS algorithms and relative error.

AM			BS		
Onwards	Backwards	Relative error	Onwards	Backwards	Relative error
0.1×10^{-23}	0.084×10^{-23}	19%	0.341×10^{-21}	0.332×10^{-21}	2.7%

Lagrange interpolation);

(iii) all the first partial derivatives as well as second- and third-order cross partial derivatives are computed at each mesh point of the grid;

(iv) then, computing the interpolated value of the function at any point just requires the determination of the elementary cube inside which the point lies and the application of the formula of the elementary cubic spline function;

(v) in the case of coordinate r, the potential is symmetric with respect to $r = 0$. All the intermediate calculations are to be done over a doubled grid to take the symmetry into account explicitly. For storage of the numerical values of the function and its derivatives, the grid can be halved.

The estimated standard deviation thus generated is 2×10^{-3} hartree.

B. Numerical integration

Two different integrators have been tested for numerical integration of the individual trajectories[35]:

(i) a seventh order Adams–Moulton–Bashforth (AM) predictor iterative corrector method,[33] based on numerical integration of the numerically interpolated function $\mathbf{f}(\tau, \mathbf{y})$ in the equation

$$\mathbf{y}(x+k) - \mathbf{y}(x) = \int_x^{x+k} \mathbf{f}(\tau, y(\tau))\, d\tau \ ,$$

which is the integral form over the propagation interval $(x, x+k)$ of the differential equation $d\mathbf{y}/d\tau = \mathbf{f}(\tau, \mathbf{y}(\tau))$;

(ii) the Bulirsch–Stoer (BS) algorithm[34] which is based on the deferred approach to the limit of an infinitely small integration step, obtained by extrapolation, developed by Richardson.

Several tests were introduced to check the numerical accuracy provided by these two methods:

1st test: Time reversal

A trajectory is integrated onwards from given initial conditions up to time τ. From that time on, conserving the positions but inverting the conjugate momenta, the same trajectory is integrated backwards. Then it is checked whether or not the trajectory reaches back the initial conditions after time τ. A typical example is as follows. Starting with the initial conditions $R^{in} = 0.9572$ Å, $r^{in} = 0$, $\alpha^{in} = 104.52°$ and all conjugate momenta equal to zero, the trajectory is inverted after $\tau = 2000$ a.u. (time step of 10 a.u.). The backwards trajectory obtained by BS works very poorly (it reaches back the area of the initial conditions after only ~1930 a.u. of time; we did not look at the accuracy of the dynamical variables). On the other hand, the AM algorithm works very well: after 2000 a.u. of time, one ends up with a situation within 2×10^{-4} a.u. for the coordinates and 7×10^{-3} a.u. for the conjugate momenta.

2nd test: Transition probabilities

The probability of remaining on the adiabatic upper surface after 2000 a.u. of time (with the same initial conditions as above) has been calculated for both the onwards and backwards trajectories. The results are given in Table II.

3rd test: Energy and angular momentum conservation

With both methods, the total angular momentum is conserved to more than six significant digits. As far as the total energy is concerned, its value is extremely well conserved by BS (within $\sim10^{-3}$ kcal/mol). To obtain the same accuracy by AM, it is necessary to reduce the time step down to 6 a.u. Then the probability of remaining on the adiabatic upper surface is 0.111×10^{-23} after 2000 a.u. of time and strictly the same for the onwards and backwards trajectories.

The concluding test is therefore to compare the computer CPU time (IBM 370/168) required by BS with $\Delta\tau = 10$ a.u. and AM with $\Delta\tau = 6$ a.u. For a given trajectory, a typical result is—8 s for BS vs 2.8 s for AM.

We thus decided to use the Adams–Moulton integrator.

C. Hamiltonian and equations of motion

$(3N-3) = 6$ generalized coordinates are used to describe the three-dimensional triatomic system including overall rotation—three Euler angles θ, ϕ, χ defined as usually (Fig. 19) and associated with the overall rotational motion, and three internal coordinates R, r, and α defined in Eqs. (2.1). The body-fixed frame bound to the molecular system is defined in Fig. 1.

By application of the matrix method introduced by Chapuisat *et al.*[36(a)] and Nauts[36(b)] to derive the Hamiltonian H and the equations of motion of a highly deformable polyatomic system described in terms of generalized coordinates, the following results were readily obtained:

Let us define the six auxiliary quantities

$$\gamma = \frac{m_H}{m_O + 2m_H} \ , \quad \gamma_1 = 1 - 2\gamma \ , \quad \gamma_c = 1 - 2\gamma\cos^2\frac{\alpha}{2} \ ,$$

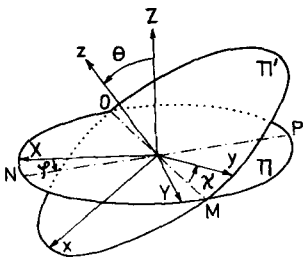

FIG. 19. Definition of the Euler angles (χ, ϕ, θ). XYZ is the space fixed frame; xyz is the body fixed frame. π is the plane containing the axes X and Y; π' is the plane containing the axes x and y. OM is the intersection between these two planes; NP is the intersection between the π plane and the plane containing the axes X and Z.

$$\gamma_s = 1 - 2\gamma \sin^2 \frac{\alpha}{2} , \quad R^* = \gamma_s R^2 + \gamma_c \frac{r^2}{4} ,$$

$$R^- = R^2 - \frac{r^2}{4} .$$

(a) The Hamiltonian function is

$$H = \frac{1}{\mu} \left\{ \tfrac{1}{2} (G_{RR} p_R^2 + G_{rr} p_r^2 + G_{\alpha\alpha} p_\alpha^2) + G_{Rr} p_R p_r + G_{R\alpha} p_R p_\alpha + G_{r\alpha} p_r p_\alpha \right\} + \tfrac{1}{2} (J_x \omega_x + J_y \omega_y + \mathcal{J}_z \omega_z) + V(R, r, \alpha)$$

$$= \frac{1}{2\mu} \langle p | G | p \rangle + \tfrac{1}{2} \langle \mathcal{J} | \omega \rangle + V , \tag{6.1}$$

where

$$\mu = m_H \gamma_1 R^*$$

and

$$G_{RR} = \left(\gamma_s^2 R^2 + \gamma_1 \frac{r^2}{4} \right) \Big/ 2 , \quad G_{rr} = 2 \left(\gamma_1 R^2 + \gamma_c^2 \frac{r^2}{4} \right)$$

$$G_{\alpha\alpha} = 2\gamma_c \gamma_s , \quad G_{Rr} = -\gamma^2 R r \sin^2 \alpha , \quad G_{R\alpha} = -\gamma \gamma_s R \sin \alpha ,$$

$$G_{r\alpha} = \gamma \gamma_c r \sin \alpha , \tag{6.2}$$

$$\mathcal{J}_z = J_z + \frac{2}{R^*} \left[\gamma \sin \alpha R^- \left(\frac{r}{4} p_R + R p_r \right) - (1 - \gamma) R r p_\alpha \right] , \tag{6.3}$$

$$\omega_x = \frac{1}{\nu \cos \frac{\alpha}{2}} \left\{ \frac{R^2 + \gamma_1 \frac{r^2}{4}}{\cos \frac{\alpha}{2}} J_x - (1 - \gamma) \frac{Rr}{\sin \frac{\alpha}{2}} J_y \right\} ,$$

$$\omega_y = \frac{1}{\nu \sin \frac{\alpha}{2}} \left\{ (1 - \gamma) \frac{Rr}{\cos \frac{\alpha}{2}} J_x + \frac{\gamma_1 R^2 + \frac{r^2}{4}}{\sin \frac{\alpha}{2}} J_y \right\} , \tag{6.4}$$

$$\omega_z = \frac{R^*}{\nu} \mathcal{J}_z .$$

Moreover,

$$\nu = 2 m_H \gamma_1 (R^-)^2 , \tag{6.5}$$

$$J_x = \sin \chi p_\theta - \csc \theta \cos \chi p_\phi + \cot \theta \cos \chi p_\chi , \tag{6.6}$$

$$J_y = \cos \chi p_\theta + \csc \theta \sin \chi p_\phi - \cot \theta \sin \chi p_\chi , \quad J_z = p_\chi .$$

(b) The equations of motion may be written as:

$$\dot{R} = \frac{1}{\mu} (G_{RR} P_R + G_{Rr} P_r + G_{R\alpha} P_\alpha) ,$$

$$\dot{r} = \frac{1}{\mu} (G_{Rr} P_R + G_{rr} P_r + G_{r\alpha} P_\alpha) , \tag{6.7}$$

$$\dot{\alpha} = \frac{1}{\mu} (G_{R\alpha} P_R + G_{r\alpha} P_r + G_{\alpha\alpha} P_\alpha)$$

(which fit in with the general relation $\mu |\dot{q}\rangle = G |P\rangle$[36])

$$\dot{\theta} = \omega^+ , \quad \dot{\phi} = \omega^- / \sin \theta , \quad \dot{\chi} = -\omega^- \cot \theta + \omega_z , \tag{6.8}$$

where

$$P_R = p_R + m_H \gamma r \sin \alpha \omega_z ,$$

$$P_r = p_r - m_H \gamma R \sin \alpha \omega_z , \tag{6.9}$$

$$P_\alpha = p_\alpha + m_H (1 - \gamma) R r \omega_z ,$$

$$\omega^+ = \sin \chi \omega_x + \cos \chi \omega_y , \quad \omega^- = -\cos \chi \omega_x + \sin \chi \omega_y . \tag{6.10}$$

In addition,

$$\dot{p}_R = -\partial H / \partial R , \quad \dot{p}_r = -\partial H / \partial r , \quad \dot{p}_\alpha = -\partial H / \partial \alpha \tag{6.11}$$

(which may straightforwardly be expressed in terms of the partial derivatives of the G's, the ω's, $\mathcal{J}_z$ and the potential energy function)

$$\dot{p}_\theta = \omega^- (\cos \theta p_\phi - p_\chi) / \sin^2 \theta , \quad \dot{p}_\phi = 0 ,$$

$$\dot{p}_\chi = \omega^- p_\theta - \omega^+ (p_\phi - \cos \theta p_\chi) / \sin \theta . \tag{6.12}$$

D. Initial conditions

The formation of H_2O^+ $(\tilde{B}\ ^2A')$ is described by Eq. (1.1). Define the absorbed energy $E_{abs} = E(H_2O^+) - E(H_2O)$. In the third band of the photoelectron spectrum of H_2O, E_{abs} ranges between 17.2 and 20.2 eV.

According to the Franck–Condon principle, there is no change in the coordinates and conjugate momenta due to electronic transitions. Thus, the distribution function which characterizes the configurational state of the H_2O^+ ion formed is the same as that of H_2O before the photon impact.

To initialize a trajectory, three kinds of variables must be specified:

(i) Phase variables that are not physically observable because of the uncertainty principle. Such variables are in the present case the initial vibrational elongations, Euler angles, and orientation of the total angular momentum vector;

(ii) The most important observable quantity (which is actually measured) in E_{abs};

(iii) In addition, there exist several variables which are physically observable, but which could not be measured in the actual experiment. Such variables are the vibrational and rotational quantum numbers v_1, v_2, v_3, and J. Since these quantities are physically informative, the numerical results will, in what follows, be discussed as a function of these quantities.

The initial conditions must describe not only the initial molecular conformation but also the initial dynamical

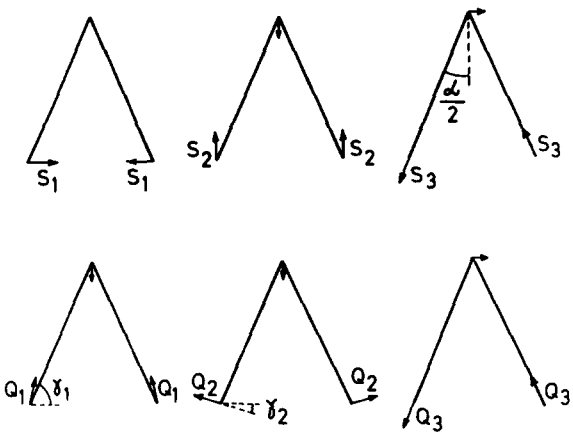

FIG. 20. Upper part: symmetry modes. The S_i's are the displacements of the hydrogen atoms in the ith symmetry mode. In the second and third symmetry modes, the displacements of the oxygen atom are equal to $(2m_H/m_O)\,S_2$ and $(2m_H/m_O)\sin(\alpha/2)S_3$, respectively. Lower part: normal modes. The Q_i's are the displacements of the hydrogen atoms in the ith normal mode. The displacements of the oxygen atom are equal to $(2m_H/m_O)\times\sin\gamma_1 Q_1$, $(2m_H/m_O)\sin\gamma_2 Q_2$, and $(2m_H/m_O)\sin(\alpha/2)Q_3$, respectively.

state, i.e., R^{in}, r^{in}, α^{in}, p_R^{in}, p_r^{in}, p_α^{in}, ϕ^{in}, θ^{in}, χ^{in}, p_ϕ^{in}, p_θ^{in}, p_χ^{in}, where the p's denote the conjugate momenta. Clearly ϕ^{in}, θ^{in}, χ^{in} are arbitrary as the overall molecular orientation is of no influence on the dynamical output of a trajectory; thus for all the trajectories, the values ϕ^{in}, θ^{in}, χ^{in} may be taken the same. On the contrary, due to possible vibration–rotation coupling effects, p_ϕ^{in}, p_θ^{in}, p_χ^{in} are not arbitrary at all. There remain therefore nine variables to initialize.

The three vibrational normal modes of H_2O ($\tilde{X}\,{}^1A'$) are assumed to be harmonic. We restrict the sampling of initial values of the normal coordinates Q_l ($l = 1, 2, 3$) to a finite range $[-Q_l^{max}, +Q_l^{max}]$ (for the choice of the Q^{max}'s, see below Sec. VI E), inside which the Q's are randomly selected (cf. Sec. VI E).

To transform the normal coordinates Q_1, Q_2, Q_3 into the internal coordinates R, r, and α, we make use of the usual symmetry coordinates S_1, S_2 and S_3[37] (Fig. 20), and for small amplitude deformations only, the result is

$$Q_1 = N_1(a\,S_1 + S_2)\ , \quad Q_2 = N_2(b\,S_1 + S_2)\ , \quad Q_3 = N_3 S_3\ . \tag{6.13}$$

The normalization coefficients N_i ($i = 1, 2, 3$) as well as the coefficients a and b are tediously, but straightforwardly obtained by solving the usual secular equation for the ground state of the neutral molecule. The intramolecular potential used is the valence-force potential of Bartlett *et al.*[38] The numerical values are

$$N_1 = 37.310\,aum^{1/2}\ , \quad N_2 = 52.337\,aum^{1/2}\ ,$$

$$N_3 = 62.922\,aum^{1/2}\ , \quad a = 1.322\,52\ , \quad b = -0.672\,118\ .$$

Hence,

$$R^{in} = R_{eq} - Q_1^{in}[A\sin(\alpha_{eq}/2) + B\cos(\alpha_{eq}/2)] + Q_2^{in}[D\sin(\alpha_{eq}/2) + E\cos(\alpha_{eq}/2)]\ , \quad r^{in} = Fv\,Q_3^{in}\ , \tag{6.14}$$

$$\alpha^{in} = \alpha_{eq} + 2\{Q_1^{in}[B\sin(\alpha_{eq}/2) - A\cos(\alpha_{eq}/2)] + Q_2^{in}[-E\sin(\alpha_{eq}/2) + D\cos(\alpha_{eq}/2)]\}/R_{eq}\ ,$$

where

$$A = [(a-b)N_1]^{-1}\ , \quad B = -buA\ , \quad D = [(a-b)N_2]^{-1}\ ,$$

$$E = -auD\ , \quad F = 2N_3^{-1}\ , \quad u = 1 + (2m_H)/m_O\ , \tag{6.15}$$

$$v = 1 + \sin^2(\alpha_{eq}/2)(2m_H)/m_O\ ,$$

and m_H and m_O are, respectively, the hydrogen and oxygen atomic masses. R_{eq} and α_{eq} are, respectively, the OH bond length and valence angle of $H_2O(\tilde{X})$ at equilibrium.

On the other hand, the momenta conjugate to R, r, and α are obtained from

$$p_q = \frac{\partial T}{\partial \dot{q}} = \sum_{i=1}^{3} \frac{\partial T}{\partial \dot{Q}_i}\frac{\partial \dot{Q}_i}{\partial \dot{q}} = \sum_{i=1}^{3} P_i \frac{\partial \dot{Q}_i}{\partial \dot{q}}\ , \quad (q = R, r, \alpha)\ ,$$

where the P_i's are the momenta conjugate to the normal coordinates Q_i's.

Hence,

$$p_R^{in} = (a-b)N_1N_2\{P_1^{in}[-E\sin(\alpha_{eq}/2) + D\cos(\alpha_{eq}/2)] - P_2^{in}[B\sin(\alpha_{eq}/2) - A\cos(\alpha_{eq}/2)]\}/u\ , \quad p_r^{in} = P_3^{in}/(vF) \tag{6.16}$$

$$p_\alpha^{in} = R_{eq}(b-a)N_1N_2\{P_1^{in}[D\sin(\alpha_{eq}/2) + E\cos(\alpha_{eq}/2)] + P_2^{in}[A\sin(\alpha_{eq}/2) + B\cos(\alpha_{eq}/2)]\}/2\ .$$

The three P_i^{in}'s are selected from quasirandom number sequences (see Sec. E). For the Q_i^{in}'s, two of them only can be selected in this way, since the value of the third one must verify the relationship

$$V_{H_2O^+(\tilde{B})}(R^{in}, r^{in}, \alpha^{in}) = V_{H_2O(\tilde{X})}(R^{in}, r^{in}, \alpha^{in}) + E_{abs} \tag{6.17}$$

according to the Franck–Condon principle. Thus, satisfying the FC principle clearly restricts the range of the possible initial conformations (see Fig. 21).

As far as the overall rotational motion is concerned, once the values of the Euler angles are fixed, there remains to specify the total angular momentum vector J.

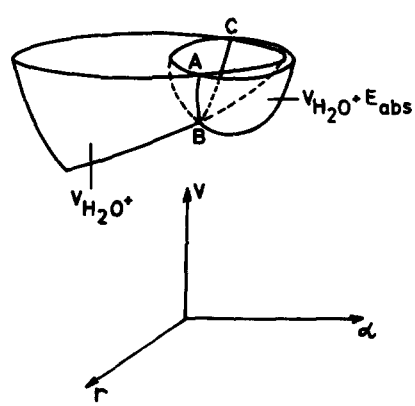

FIG. 21. Application of the Franck–Condon principle leads to possible initial conformations of H_2O^+ which are located on the curve ABC, i.e., on the intersection between $V_{H_2O^+}$ and $(V_{H_2O^+}+E_{abs})$.

In terms of the rotational quantum number J, this is given by

$$\|\mathbf{J}\| = \hbar \sqrt{J(J+1)} \ .$$

The orientation of J can be specified by means of two randomly selected polar angles Θ and Φ (cf. paragraph *E*), so that:

$$J_x^{in} = \|\mathbf{J}\| \sin\Theta^{in} \cos\Phi^{in} \ , \quad J_y^{in} = \|\mathbf{J}\| \sin\Theta^{in} \sin\Phi^{in} \ ,$$

$$J_z^{in} = \|\mathbf{J}\| \cos\Theta^{in} \ .$$

The quantities actually needed to initialize the equations of motion [see Eq. (6.1)] are p_ϕ^{in}, p_θ^{in}, p_χ^{in}. According to the usual transformation[39] the result is

$$p_\phi^{in} = \sin\theta^{in}(\sin\chi^{in} J_y^{in} - \cos\chi^{in} J_x^{in} + \cot\theta^{in} J_z^{in}) \ ,$$

$$p_\theta^{in} = \sin\chi^{in} J_x^{in} + \cos\chi^{in} J_y^{in} \ , \quad p_\chi^{in} = J_z^{in} \ . \tag{6.18}$$

E. Average over the individual trajectories

1. Numerical integration

The numerical results are to be integrated over the range of variation of variables of types (i) and (ii) in order to obtain average values. In particular, the overall transition probability for the nonadiabatic process $\tilde{B} \to \tilde{A}$, $\bar{P}_{tr}$ is at given E_{abs}:

$$\bar{P}_{tr}(\tau; v_1, v_2, v_3, J, E_{abs}) = \frac{\int d\omega f(\omega; v_1, v_2, v_3, J, E_{abs}) p(\tau; \omega)}{\int d\omega f(\omega; v_1, v_2, v_3, J, E_{abs})} \ , \tag{6.19}$$

where τ is the time, ω a set of initial conditions for phase variables, $f(\omega; v_1, v_2, v_3, J, E_{abs})$ the statistical weight of the trajectory proceeding from the initial conditions ω, whose transition probability throughout the time is $p(\tau;\omega)$. In addition, from $\bar{P}_{tr}(\tau; v_1, v_2, v_3, J, E_{abs})$ it is possible to derive $k(v_1, v_2, v_3, J, E_{abs})$, the rate constant of process $\tilde{B} \to \tilde{A}$ at given E_{abs} (see below, Sec. VI G). The average rate constant $k(v_1, v_2, v_3, J)$ is obtained by integration over E_{abs}:

$$k(v_1, v_2, v_3, J) = \frac{\int dE_{abs} k(v_1, v_2, v_3, J, E_{abs}) I(E_{abs})}{\int dE_{abs} I(E_{abs})} \ , \tag{6.20}$$

where $I(E_{abs})$ is the intensity of the photoelectron spectrum at E_{abs}.

Equation (6.19) involves a multiple integration process. The integrand is not known analytically, but numerically for various values of ω. In such a case, it is most efficient to numerically integrate by using a Monte Carlo type method[40]:

$$I = \int_0^1 \int_0^1 \cdots \int_0^1 F(x_1, x_2 \ldots x_k)\, dx_1 dx_2 \cdots dx_k$$

$$\approx N^{-1} \sum_{i=1}^{N} F(x_1^i, x_2^i \cdots x_k^i) \ , \tag{6.21}$$

where the N points $(x_1^i, x_2^i \ldots x_k^i)$ $(i = 1, \ldots N)$ are randomly selected inside the unit hypercube. Obviously, it is always possible to reduce an integral over a nonunit interval to one over a unit interval by means of scaling factors. Unfortunately, the series in Eq. (6.21) converges rather poorly. Thus, in order to improve the convergence, various methods have been proposed, based on either quasirandom or nonrandom sequences. In what follows, we have chosen the Halton sequences,[35,41] rather similar to the Hammersley sequences, which generate quasirandom numbers in the range 0–1. Let us denote a set of k Halton sequences associated with k variables and running over N points [cf. the series in Eq. (6.21)] by

$$\{x_r^i \ ; \ r = 1, 2 \ldots k \ ; \ i = 1, 2 \ldots N\} \ ,$$

where x_r^i lies in the range $[0, 1]$.

Within the context of the present dynamical study, the Halton sequences randomly select initial conditions from which trajectories are run. The numerical results of all these trajectories are to be averaged by taking into account the statistical weight of each trajectory.

The initial conditions in terms of normal coordinates and conjugate momenta are randomly selected as follows (for the ith trajectory out of a set of N trajectories):

$$Q_r^{in} = x_r^i Q_r^{max} (-1)^{u_r} \ , \quad (r = 1, 2) \ ,$$

$$P_r^{in} = x_{r+2}^i P_r^{max} (-1)^{u_{r+2}} \ , \quad (r = 1, 2, 3) \ ,$$

$$\Theta^{in} = 2\pi x_6^i \ , \tag{6.22}$$

$$\Phi^{in} = 2\pi x_7^i \ ,$$

where $u_r = 1$ if $x_{r+7}^i < 0.5$ and $u_r = 0$ if $x_{r+7}^i > 0.5$ $(r = 1, 2 \ldots 5)$ in order to take into account the fact that the Q's and P's can be either positive or negative. As shown above (cf. Sec. VI D) the initial conditions in terms of the variables used to propagate the trajectories can be obtained from Eqs. (6.14), (6.16), and (6.17). Up to now 12 random numbers have been used; a 13 one is needed to specify the plus or minus sign of r^{in}, the third initial coordinate obtained by Eq. (6.17) to satisfy the FC principle.

2. Distribution functions and statistical weights

Because of the isotropy of space, all the orientations of J are equally probable. Therefore, the statistical weight to be associated with a given trajectory depends (v_1, v_2, v_3, J, and E_{abs} being fixed) only on the initial values of the vibrational coordinates and conjugate momenta. It is by now well established that the Wigner "distribution function"[42] works reasonably well in such a case, in spite of the drawback that it may not be positive everywhere. Its main advantage is that, integrated over the momenta, it gives the correct quantum mechanical density function for the coordinates and, integrated over the coordinates, the correct density function for the momenta. In our case, it is defined by

$$W_{v_1, v_2, v_3}(Q_1, Q_2, Q_3, P_1, P_2, P_3) = (\pi\hbar)^{-3} \iiint_{-\infty}^{+\infty} dy_1 dy_2 dy_3 \, \psi^*_{v_1, v_2, v_3}(Q_1 + y_1, Q_2 + y_2, Q_3 + y_3)$$

$$\times \psi_{v_1, v_2, v_3}(Q_1 - y_1, Q_2 - y_2, Q_3 - y_3) \exp[2i(P_1 y_1 + P_2 y_2 + P_3 y_3)/\hbar] \ .$$

TABLE III. Results for H_2O in its vibrational ground state with the potential used taken into account.

i	Q_i^{max} (a.u.)	P_i^{max} (a.u.)
1 Symmetric stretching	13.1	0.230
2 Bending	19.8	0.152
3 Antisymmetric stretching	12.9	0.232

For harmonic vibrations, Bartlett and Moyal[43] have shown that the Wigner function associated with one normal mode is

$$W_{v_i}(Q_i, P_i) = (\pi\hbar)^{-1}(-1)^{v_i} L_{v_i}(2X_i)\exp(-X_i) ,$$

where

$$X_i = (\lambda_i^{1/2}Q_i^2 + \lambda_i^{-1/2}P_i^2)/\hbar , \quad \lambda_i = 4\pi^2\omega_i^2 ,$$

and ω_i is the vibrational frequency of the ith normal mode. L_{v_i} denotes a Laguerre polynomial of degree v_i. Clearly, because of the separation of the normal vibrations,

$$W_{v_1,v_2,v_3}(Q_1, Q_2, Q_3, P_1, P_2, P_3) = W_{v_1}(Q_1, P_1)W_{v_2}(Q_2, P_2)W_{v_3}(Q_3, P_3) .$$

For the fundamental vibrational state, the Wigner function happens to be the product of the true density function for the coordinates by that for the momenta.

Recently, Heller[44] showed that using the Wigner function results is a much better pseudoclassical dynamical method than the purely classical dynamical treatment. Moreover, Fiquet-Fayard *et al.*[45] compared quantum-mechanical results with various classical results for the same problem; they concluded that only the classical method that made use of Wigner functions led to results in good agreement with the quantal results.

Last of all, the boundaries Q_i^{max} and P_i^{max} for given v_i which appear in Eqs. (6.22) are determined from the study of the variations of the functions $W_{v_i}(Q_i, 0)$ and $W_{v_i}(0, P_i)$, in the following way: the maximal values of these two functions being calculated, Q_i^{max} and P_i^{max} are chosen in those variation domains where the functions monotonically tend to zero, in such a way that $W_{v_i}(Q_i^{max}, 0)/\max[W_{v_i}(Q_i, 0)]$ and $W_{v_i}(0, P_i^{max})/\max[W_{v_i}(0, P_i)] < 0.05$. For H_2O in its vibrational ground state and taking into account the potential used, the results are listed in Table III.

F. The nonadiabatic transition model

It has been shown above (cf. part IV) that the transition probability $\tilde{B} \to \tilde{A}$ reasonably obeys the Nikitin formula [Eq. (5.4)]. This means that, for a particular trajectory, the transition probability must be calculated with quantities evaluated at the particular point where the difference between the adiabatic states (i.e., ΔE) is minimal. Only in the case of a Jahn–Teller interaction does this point coincide with the point where the distance of nearest approach to the apex of the cone is minimal.

As the lower adiabatic surface E_1 is not stored in our case, ΔE cannot be known. As a consequence, the elementary transition probability must be evaluated at another point of the trajectory. Two models were compared.

In the first model, the quantities in Eq. (5.4) were evaluated at the seam $\alpha = \alpha_c(R)$ for every passage through it. For those trajectories that never cut the seam, the transition is localized at the point (R, r, α) which minimizes the distance to the apex of the cone $d = [R^2(\alpha - \alpha_c(R))^2 + r^2]^{1/2}$.

In the second model, these quantities were evaluated at the distance of nearest approach to the apex of the cone, calculated for every half-oscillation of the internal coordinate α.

The calculations were performed at time $\tau = 600$ a.u. and $E_{abs} = 18.5$ eV. The results are as follows: In the case of the first model, $\bar{P}_{tr} = 0.66$ and in the case of the second model, $\bar{P}_{tr} = 0.63$. The difference is not important and the first model was adopted for all the other calculations.

The transition probability $\tilde{B} \to \tilde{A}$ associated with a given trajectory under initial conditions ω is:

$$p_{tr}(\omega, \tau) = 1 - \prod_{i=1}^{n_\tau} [1 - p_i(\omega)] ,$$

when n_τ indicates how many times the seam has been gone through and $p_i(\omega)$ is the elementary transition probability obtained as explained above. p_{tr} is a function of time because the longer the trajectory lasts the larger n_τ is.

For a set of N trajectories whose initial conditions ω_j ($j = 1, 2, \ldots, N$) have been randomly selected, the averaged time-dependent transition probability is given by:

$$\bar{P}_{tr}(\tau; v_1, v_2, v_3, J, E_{abs}) \approx \frac{\sum_{j=1}^{N} W_{v_1v_2v_3}(\bar{\omega}_j)\, p_{tr}(\omega_j; \tau)}{\sum_{j=1}^{N} W_{v_1v_2v_3}(\bar{\omega}_j)} ,$$

where $\bar{\omega}_j$ denotes $(Q_1^{in}, Q_2^{in}, Q_3^{in}, P_1^{in}, P_2^{in}, P_3^{in})$ for the jth trajectory and ω_j is $\bar{\omega}_j$ plus p_ϕ^{in}, p_θ^{in}, p_χ^{in}. It should be emphasized that ω_j is implicitly a function of J and E_{abs}. Obviously, $\lim_{\tau\to\infty}[\bar{P}_{tr}(\tau, \ldots)] = 1$ because the flow from $\tilde{B}$ to $\tilde{A}$ will necessarily be complete at long last.

G. Rate constant for the nonadiabatic process $\tilde{B} \to \tilde{A}$

If the nonadiabatic process $\tilde{B} \to \tilde{A}$ can be treated as a unimolecular reaction, the flow to the lower surface will obey a rate equation of the form

$$\ln([A]/[A]_0) = -k\tau ,$$

where k is the rate constant and the concentrations $[A]$ and $[A]_0$ correspond to the population of the $\tilde{B}$ state at time τ and $\tau = 0$, respectively. Within the framework of the present study, this assumption leads to

$$\ln[1 - \bar{P}_{tr}(\tau; v_1, v_2, v_3, J, E_{abs})] = -k(v_1, v_2, v_3, J, E_{abs})\tau , \quad (6.2)$$

$\ln(1 - \bar{P}_{tr})$ being proportional to τ, or not, will be a

test of validity for the unimolecular character of the decay.

The rate constant averaged over the energy range of the third band of the photoelectron spectrum of $H_2O(\tilde{X})$, $\bar{k}(v_1, v_2, v_3, J)$ can be derived from Eq. (6.20).

VII. DYNAMICAL STUDY: NUMERICAL RESULTS

Although the experimental results we have at our disposal were not obtained for given initial internal states of the water molecule, the photochemical process which we discuss below can be written as

$$H_2O(\tilde{X}; J, v_1, v_2, v_3) \xrightarrow{E_{abs}} H_2O^*(\tilde{B}) \xrightarrow[\text{transition}]{\text{nonadiabatic}} H_2O^*(\tilde{A}) \rightarrow \text{products} ,$$

i.e., a completely determined process. The discussion below deals with the various aspects of this reaction, namely: (i) a study of the influence of the initial internal state of H_2O, specified by J, v_1, v_2, and v_3; (ii) a study of the efficiency of the nonadiabatic transition process and a derivation of a rate constant; and (iii) a study of the influence of E_{abs} on the value of this rate constant, over the whole range of the third band of the photoelectron spectrum of H_2O.

A. Influence of the initial internal state of H_2O

The present study is based on transition probabilities calculated at a particular time $\tau = 400$ a.u., because the cumulative transition probability is then in most cases of the order of 0.5, and at an energy E_{abs} equal to 18.5 eV, corresponding to the maximum intensity of the third band of the photoelectron spectrum.

The influence of v_1, v_2, v_3, and J on the transition probability is then studied by considering a number of cases:

(i) v_1, v_2, $v_3 = 0$, and J successively equal to 0, 1, 2, 3, 5, 6, 8, 10, 20;

(ii) $v_2 = v_3 = 0$; $v_1 = 0$ and 3; $J = 3$ and 10;

(iii) $v_1 = v_2 = 0$; $v_3 = 0$, 1, 3 and 5; $J = 3$ and 10;

(iv) $v_1 = v_3 = 0$; $v_2 = 0$ and 5; $J = 3$ and 10.

The number of trajectories used to calculate $\bar{P}_{tr}$ ranged between 130 and 220; this ensured an accuracy of 2%. The results are presented in Table IV.

Case (a): *Influence of* J. The influence of the initial rotational state of H_2O was found to be almost negligible in all cases, except when $v_3 = 5$, i.e., when the antisymmetric stretching mode is strongly excited.

Case (b): *Influence of* v_1. The excitation of the symmetric stretching mode of H_2O from $v_1 = 0$ to $v_1 = 3$ lowers the transition probabilities for $J = 3$ as well as for $J = 10$. This can be traced back to the fact that, the higher v_1, the larger the average absolute value $\bar{r}_c$ of the intercept of the trajectory with the seam ($\bar{r}_c \simeq 0.19$ or 0.36 Å for $v_1 = 0$ or 3, respectively). In other words, this effect is due to the coupling between the symmetric and the antisymmetric stretching modes induced by the potential.

Case (c): *Influence of* v_3. The excitation of the antisymmetric stretching mode lowers the transition probability, but the effect is much more pronounced than in case (b). The same kind of argument (increase of $\bar{r}_c$) can be invoked. However, in the previous case, the influence is due to coupling effects and therefore is indirect. In the present case, the increase of $\bar{r}_c$ is a direct consequence of the excitation of the antisymmetric mode. Indeed, $\bar{r}_c = 0.19$ Å for $v_3 = 0$, and $\bar{r}_c = 1.27$ Å for $v_3 = 5$. As a result, the transition probability falls off by a factor of ten.

Case (d): *Influence of* v_2. An increase of v_2 from 0 to 5 has an almost negligible influence on $\bar{r}_c$ (0.19 and 0.21 Å, respectively). Consistently, the influence on the transition probability is very small. This is indicative of a small potential coupling between r and α.

B. Rate of decay

In order to test the unimolecular character of the decay, $\ln(1 - \bar{P}_{tr})$ was computed and plotted as a function of time according to Eq. (6.23). Results at three energies E_{abs} are given in Figs. 22–24. The nonlinear character of these curves clearly indicates that our previous assumption (Sec. VI G) of the decay being purely unimolecular is somewhat oversimplified. This clearly results from the fact that we could study the

TABLE IV. Numerical values of $\bar{P}_{tr}$ at $\tau = 400$ a.u. and $E_{abs} = 18.5$ eV, for several values of the quantum numbers J, v_1, v_2, v_3 of H_2O before photon impact.

J	v_1	v_2	v_3	$\bar{P}_{tr}$
0,1,2,3	0	0	0	0.57
5,6,8	0	0	0	0.56
10	0	0	0	0.58
20	0	0	0	0.60
3	3	0	0	0.42
10	3	0	0	0.43
3	0	5	0	0.61
10	0	5	0	0.61
3	0	0	1	0.40
10	0	0	1	0.42
3	0	0	3	0.26
10	0	0	3	0.25
3	0	0	5	0.06
10	0	0	5	0.15

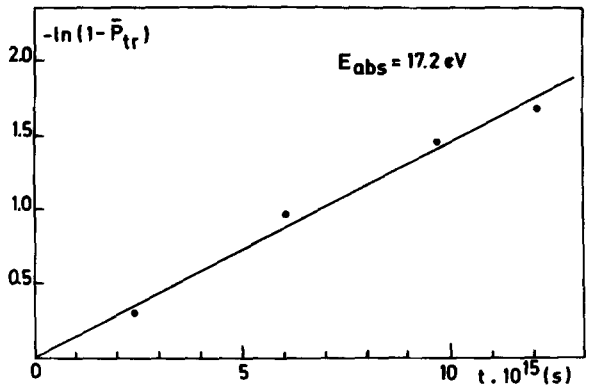

FIG. 22. Function $-\ln(1-\bar{P}_{tr})$ vs time $\tau(s)$ for $E_{abs}=17.2$ eV. The dots are the numerical values and the full line is the best straight line fit to them. $v_1=v_2=v_3=0$ and $J=3$ are, respectively, vibrational and rotational quantum numbers.

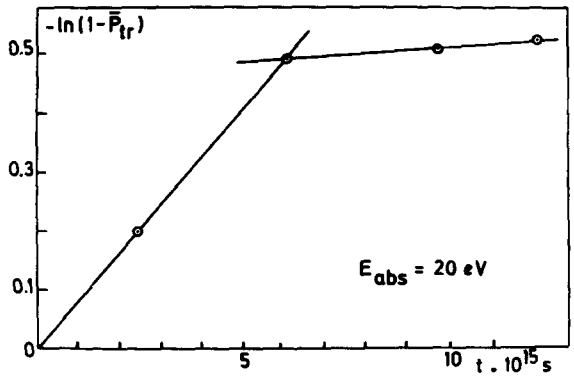

FIG. 24. Function $-\ln(1-\bar{P}_{tr})$ vs time $\tau(s)$ for $E_{abs}=20$ eV. The dots are the numerical values and the full lines are the best straight line fits obtained for the short time and intermediate time ranges. $v_1=v_2=v_3=0$ and $J=3$ are, respectively, vibrational and rotational quantum numbers.

system only up to a time equal to 2.5×10^{-14} s. The kinetic regime is thus not yet established.

The behavior of the curves in Figs. 22–24 can, however, be rationalized as follows. Several parts, with different slopes, can be distinguished in these curves.

At very short times, the slope is negligible since no trajectroy has yet reached the region of the conical intersection. No transition thus occurs.

Next, at short times, the slope rapidly increases. This is due to those trajectories that have a negligible amount of energy in the r degree of freedom and thus reach very rapidly the region of nonadiabaticity. $\bar{P}_{tr}$ is then very large as these trajectories pass close to the apex of the cone [cf. Eq. (5.4)]. Hence, the increase of the slope. Within the framework of the surface hopping model, this type of trajectory does not undergo branching at the crossing region. This is schematically represented in Fig. 25(a). This behavior persists up to about 5×10^{-15} s, corresponding roughly to the time during which the HOH valence angle closes from its initial value ($\simeq 105°$) down to its value at the seam ($\simeq 80°$).

Trajectories for which there is some energy in coordinate r reach the nonadiabatic region after the previous ones, and furthermore undergo splitting since their distance of nearest approach to the apex of the cone is larger [see Fig. 25(b)]. As a consequence, depopulation of the upper state is less rapid, which accounts for the relative flatness of the curve in Fig. 23 up to about $1.5\ 10^{-14}$ s.

As shown in Fig. 25(c), this limit of 1.5×10^{-14} s corresponds to a time when the trajectories which remain on the upper adiabatic potential (the only ones which were actually calculated) come back towards the zone of nonadiabatic interaction with dynamical conditions which allow them to branch to the lower sur-

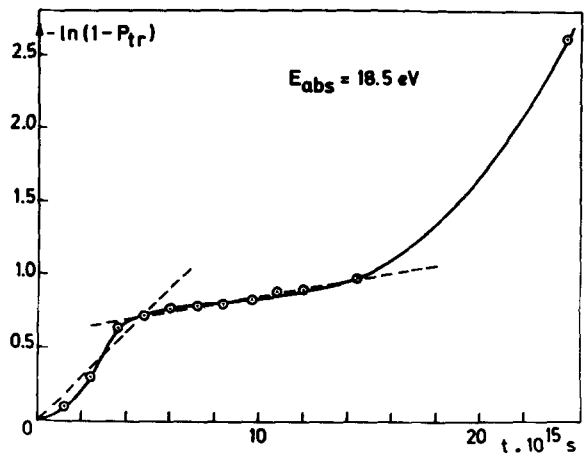

FIG. 23. Function $-\ln(1-\bar{P}_{tr})$ vs time $\tau(s)$ for $E_{abs}=18.5$ eV. The dots are the numerical values and the dashed lines are the best straight line fits obtained for the short time and intermediate time ranges, respectively. $v_1=v_2=v_3=0$ and $J=3$ are, respectively, vibrational and rotational quantum number.

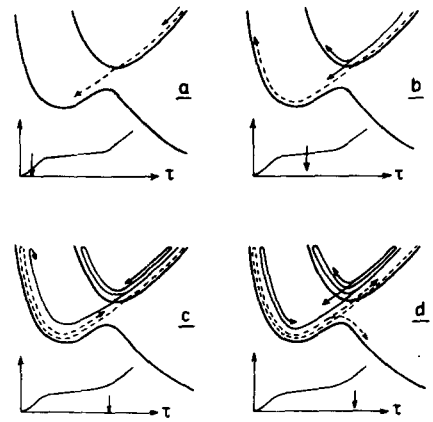

FIG. 25. Schematic view, at four different times τ, of the evolution of the flux of trajectories on the potential energy surfaces (represented in one dimension only). The dashed line represents the evolution of the set of trajectories that are initially the most efficient and which rapidly reach the region of strong coupling. The full line represents the evolution of the other set of trajectories which are less efficient and which reach the region of strong coupling more slowly.

face. [We neglect here the first bounce back on the steep inner wall of the upper surface which takes place at $\simeq 7\times10^{-15}$ s. The reason is that, since the potential is very steep, the dynamical conditions remain practically unchanged (Fig. 26). Hence, if the inward motion could not bring about a substantial nonadiabatic transition, the same situation will prevail for the outward passage which takes place immediately after.]

Therefore, a substantial source of depopulation of the upper state sets in at times larger than 1.5×10^{-14} s. Hence, the slope of the graph [Eq. (6.23)] suddenly increases after this time (Fig. 23). However, this effect might be spurious, since it is counteracted by an opposing effect which was not taken into account in our calculations. It turns out that trajectories which result from motion on the lower adiabatic surface come back in the vicinity of the apex of the cone at about the same time (1.5×10^{-14} s). The population of the upper state increases by this nonadiabatic effect, i.e., it decreases less rapidly than predicted by our calculations. In other words, the slope calculated at times longer than 1.5×10^{-14} s is overestimated. It is conceivable that the two effects cancel to a larger degree and that no change in the slope would appear in a more exact calculation. If the trajectories had been calculated during a longer period of time with all the opposing effects duly taken into account, a correct value of the slope would have been obtained. However, there is little point in attempting to study the behavior of the system at longer times, because, owing to the great efficiency of the mechanism, the upper state depopulates very fast.

C. Influence of E_{abs} on the rate constant

As explained before and as shown in Figs. 23 and 24, it appears that the depopulation of the upper adiabatic state E_2 towards the lower state E_1 presents two distinct regimes, for short and intermediate time ranges, respectively. This is the reason why the graphs in Figs. 23 and 24 are approximated by two segments of a straight line, the slopes of which are denoted by k_1 (short time range) and k_2 (intermediate time range). The values of k_1 and k_2 are calculated for five values of E_{abs} and are presented in Table V.

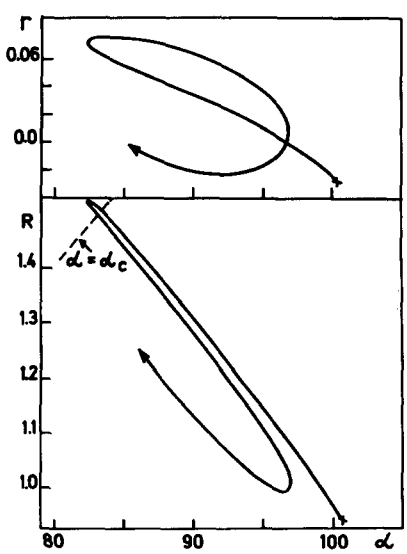

FIG. 26. Upper part: variation of the averaged value of r(Å) vs the averaged value of α (deg), for a set of trajectories whose initial conditions have been randomly selected with $J=3$, $v_1=v_2=v_3=0$, $E_{abs}=18.5$ eV and $\tau=740$ a.u. Lower part: variation of the averaged value of R(Å) vs the averaged value of α (deg) for the same set of trajectories as in the upper part.

TABLE V. Rate constants (s^{-1}) for short time range (k_1) and intermediate time range (k_2) for five values of E_{abs} (eV).

E_{abs}	k_1	k_2
17.2	1.46×10^{14}	1.46×10^{14}
17.8	2.00×10^{14}	0.80×10^{14}
18.5	1.51×10^{14}	0.28×10^{14}
19.1	1.33×10^{14}	0.15×10^{14}
20.0	0.81×10^{14}	0.05×10^{14}

1. Short time range: $k_1(E_{abs})$

From Table V, it appears that k_1 first increases, then decreases as a function of E_{abs}.

As discussed before, k_1 represents the efficiency of a few trajectories that are characterized by very little internal energy in the r coordinate. Since r remains negligible throughout, such trajectories pass very close to the apex of the cone, just as in a diatomic case where the trajectories would pass through the intersection between the two states under consideration. Thus, it can be said that those trajectories have a diatomiclike behavior. Hence, as E_{abs} (i.e., the total internal energy) increases, the nuclear velocity in the coupling region increases too, and so does the transition probability. This accounts for the initial increase of k_1 as a function of E_{abs}.

However, when the total internal energy becomes sufficiently large, a substantial part of it can convert to potential energy stored in the r coordinate, which thus can take larger values. The system tends to pass farther away from the apex of the cone and the depopulation of state E_2 slows down. This accounts for the subsequent decrease of k_1 as a function of E_{abs}.

2. Intermediate time range: $k_2(E_{abs})$

As explained before, most of the trajectories reach the coupling region with a large "impact parameter" to the apex of the cone. These trajectories have a typical polyatomic behavior.

As E_{abs} increases, r is allowed to take larger values, i.e., the impact parameter to the apex of the cone increases and, correspondingly, the transition probability decreases. Thus, k_2 decreases as a function of E_{abs}, as may be seen in Table V.

3. Average over E_{abs}

The averaged rate constants k_1 and k_2 over E_{abs} are obtained by integration

TABLE VI. Percentage x_n of trajectories for which n percents of the internal energy, initially in R and α only, have been converted into potential energy of the r coordinate, for three values of time τ (a.u.).

τ	x_{25}	x_{33}	x_{50}	x_{80}
200	19%	15%	9%	1%
400	49%	40%	27%	15%
600	50%	40%	27%	16%

$$\bar{k}_i = \frac{\int dE_{abs}\, k_i(E_{abs}) I(E_{abs})}{\int dE_{abs}\, I(E_{abs})} \quad , \quad i = 1,\ 2 \ ,$$

where $I(E_{abs})$ is the intensity of the photoelectron spectrum of H_2O, at given E_{abs}. Numerical integration leads to the following numerical values:

$$\bar{k}_1 = 1.53 \times 10^{14}\ s^{-1} \ , \quad \bar{k}_2 = 0.36 \times 10^{14}\ s^{-1} \ .$$

D. Energy randomization

The optical selection rule allows the two totally symmetric vibrational degrees of freedom Q_1 and Q_2 (corresponding roughly to R and α) to receive internal energy from the photon field, whereas Q_3 cannot do so for symmetry reasons. The question then arises how fast will energy flow into the optically inactive degree of freedom Q_3 as a result of the anharmonic nature of the potential energy surface?

To answer this question, we have calculated, as a function of time τ, the fraction x_n of trajectories for which coordinate r reaches at least once a value such that $n\%$ of the total internal energy has converted into potential energy stored in the r coordinate. For example, at $E_{abs} = 18.5$ eV, a value of $r = 0.56$ Å means that the r coordinate has received all of the available internal energy. A value of $r = 0.4$ Å means that 50% of the internal energy has flowed into Q_3. Values of $r = 0.34$ and 0.3 Å correspond to the conversion of 33% and 25%, respectively, of the internal energy into potential energy of the r coordinate.

Calculations were done for three values of τ equal to 200, 400, and 600 a.u. (i.e., 0.48, 0.97, and 1.45×10^{-14} s). Results are given in Table VI.

The system cannot be said to be randomized unless at least one-third of the total internal energy has flowed into the r coordinate as potential energy. This is a necessary but not sufficient criterion for energy randomization.

Table VI shows that after a time $\tau = 600$ a.u. $= 1.45 \times 10^{-14}$ s. i.e., after a time which is of the order of a typical vibrational period, 40% of the trajectories have already satisfied this requirement. But the further evolution is seen to be much slower, and a state of full randomization might be only obtained after a considerably longer period of time, provided, of course, that the system has not dissociated before. Obviously, this particular example represents an "easy case" since energy has to get randomized among three degrees of freedom only, out of which two have already received a substantial amount of energy at time $\tau = 0$ (photon impact) as a result of the optical selection rules.

VIII. CONCLUSIONS

The importance of conical intersections in accounting for the reactivity of excited electronic states has been repeatedly demonstrated.[3-5,8-11,46] In the present article, we have tried to extend to unimolecular reactions the effort which has been directed towards understanding bimolecular processes.[47] Although it is not advisable to draw too many conclusions from only one example, we list here our principal findings:

(i) The accuracy of the linear model (cf. Fig. 10) over a fairly important range of coordinates in spite of the curvature of the diabatic surfaces. This conclusion is corroborated by similar tests on other molecules[8(b),11];

(ii) The validity of the Landau–Zener model in Nikitin's bidimensional version as demonstrated by the appropriate behavior of the global functions $t(s)$ and $T(S)$ (cf. Figs. 13–16);

(iii) The magnitude of the unimolecular rate constant describing the internal conversion from the upper cone to the lower adiabatic surface. The high value obtained ($\simeq 10^{14}\ s^{-1}$) is typical of a fast radiationless process;

(iv) The relative insensitivity of this rate constant to the initial amount of rotational and bending vibrational energy (whereas excitation of the stretching modes lowers the transition probability).

(v) An entirely unsuspected bimodal behavior of this radiationless transition for which the existence of two regimes was recognized (cf. Figs. 23 and 24):

(a) a short-time regime corresponding to a fast, nonstatistical, diatomiclike process;

(b) a somewhat slower regime, presumably due to the multidimensional character of the trajectories;

(vi) A rapid initial tendency towards energy randomization followed by a slower evolution towards a state of microcanonical equilibrium. This suggests that a statistical treatment might be applied, at least in cases where the dissociation process is not too rapid. This possibility is currently investigated in this laboratory.

As far as the photodecomposition of H_2O at $h\nu \approx 18.5$ eV is concerned, it seems now well established that the nonadiabatic passing through the conical intersection between the $\tilde{B}$ and $\tilde{A}$ states of H_2O^* plays an important role in producing the surprisingly large amount of H^* observed. It seems to be at least competitive with the previously proposed electronic predissociations of the $\tilde{B}$ state of H_2O^* by two repulsive states, $^2A''$ and $^4A''$, for production of, respectively, H^* and OH^*.

ACKNOWLEDGMENTS

The authors wish to thank Dr. C. Leforestier for the spline interpolation, Adams–Moulton and Bulirsch–Stoer integration subroutines and Dr. S. Goursaud for

providing them with a Halton sequences generator subroutine. They are indebted to Dr. M. Baer for a helpful communication about the multivaluation of the function θ. One of us (D. D.) is grateful to the "Fonds National de la Recherche Scientifique" and to the "Institut pour l'Encouragement de la Recherche Scientifique dans l'Industrie et l'Agriculture" for a fellowship. This work has been supported by the Belgian Government (Action de Recherche concertée), the "Fonds de la Recherche Fondamentale Collective," and the French C.N.R.S.

[1](a) R. N. Porter, Annu. Rev. Phys. Chem. **25**, 317 (1974); (b) X. Chapuisat and Y. Jean, Top. Cur. Chem. **68**, 1 (1976).
[2]*Dynamics of Molecular Collisions*, edited by W. H. Miller (Plenum, New York, 1976), part B.
[3]E. E. Nikitin, in *Chemische Elementarprozesse*, edited by H. Hartmann (Springer, Berlin, 1968), p. 70; *Theory of Elementary Atomic and Molecular Processes in Gases*, translated by M. J. Kearsley (Clarendon, Oxford, 1974); E. E. Nikitin and L. Zülicke, *Selected Topics of the Theory of Chemical Elementary Processes* (Springer, Berlin, 1978).
[4]R. K. Preston and J. C. Tully, J. Chem. Phys. **54**, 4297 (1971); J. C. Tully and R. K. Preston, *ibid.* **55**, 562 (1971).
[5]J. C. Tully, in *Dynamics of Molecular Collisions*, edited by W. H. Miller (Plenum, New York, 1976), p. 217.
[6]W. G. Dauben, L. Salem, and N. J. Turro, Acc. Chem. Res. **8**, 41 (1975); J. Michl, Top. Curr. Chem. **46**, 1 (1974).
[7]A. Warshel and M. Karplus, Chem. Phys. Lett. **32**, 11 (1975); A. Warshel, Nature (London) **260**, 679 (1976); J. Am. Chem. Soc. **101**, 6131 (1979).
[8](a) C. Galloy and J. C. Lorquet, J. Chem. Phys. **67**, 4672 (1977); (b) J. C. Lorquet, C. Sannen, and G. Raseev, J. Am. Chem. Soc. **102**, 7976 (1980); C. Sannen, G. Raseev, C. Galloy, G. Fauville, and J. C. Lorquet, J. Chem. Phys. **74**, 2402 (1981).
[9]J. C. Lorquet, C. Galloy, M. Desouter-Lecomte, M. J. Decheneux, and D. Dehareng, in *Excited States in Organic Chemistry and Biochemistry*, edited by B. Pullman and N. Goldblum (Reidel, Dordrecht, 1977), p. 397.
[10]M. Desouter-Lecomte and J. C. Lorquet, J. Chem. Phys. **71**, 4391 (1979).
[11]M. Desouter-Lecomte, C. Galloy, J. C. Lorquet, and M. Vaz Pires, J. Chem. Phys. **71**, 3661 (1979).
[12]H. Hellman and J. K. Syrkin, Acta Physicochim. URSS **2**, 433 (1935).
[13]F. T. Smith, Phys. Rev. **179**, 111 (1969).
[14]F. Fiquet-Fayard and P. M. Guyon, Mol. Phys. **11**, 17 (1966).
[15]J. C. Leclerc, J. A. Horsley, and J. C. Lorquet, Chem. Phys. **4**, 337 (1974).
[16]A. J. Lorquet and J. C. Lorquet, Chem. Phys. **4**, 353 (1974).
[17]J. H. D. Eland, Chem. Phys. **11**, 41 (1975).
[18]G. G. Balint-Kurti and R. N. Yardley, Chem. Phys. Lett. **36**, 342 (1975).
[19]J. A. Smith, P. Jørgensen, and Y. Ohrn, J. Chem. Phys. **62**, 1285 (1975).
[20]R. A. Rouse, J. Chem. Phys. **64**, 1224 (1976).
[21]P. J. Fortune, B. J. Rosenberg, and A. C. Wahl, J. Chem. Phys. **65**, 2201 (1976).
[22]C. F. Jackels, J. Chem. Phys. **72**, 4873 (1980).
[23]J. B. Delos and W. R. Thorson, Phys. Rev. A **6**, 728 (1972).
[24]S. Huzinaga, J. Chem. Phys. **42**, 1293 (1965).
[25]J. H. Dunning, J. Chem. Phys. **53**, 2823 (1970).
[26]R. McWeeny, Mol. Phys. **28**, 1273 (1974); L. Salem, C. Leforestier, B. Segal, and R. Wetmore, J. Am. Chem. Soc. **97**, 479 (1975); J. Lievin and G. Verhaegen, Theor. Chim. Acta **42**, 42 (1976).
[27]The program system MOLALCH incorporates the MOLECULE Gaussian integral program and the ALCHEMY SCF and CI wave function generator programs. MOLECULE was written by Dr. J. Almlöf of the University of Uppsala, Sweden. ALCHEMY was written at the IBM San Jose Research Laboratory. The interfacing of these programs was performed by P. S. Bagus and U. I. Wahlgren. For a description of MOLECULE see J. Almlöf, *Proceedings of the Second Seminar on Computational Problems in Quantum Chemistry* (Max Planck Institute, München, 1973), p. 14. For a description of ALCHEMY, see P. S. Bagus, in *Selected Topics in Molecular Physics* (Chemie, Weinheim, 1972), p. 187.
[28]P. M. Prenter, *Splines and Variational Methods* (Wiley, New York, 1975).
[29]P. O. Löwdin, Phys. Rev. **97**, 1495 (1955).
[30]P. S. Bagus, B. Liu, A. D. McLean, and M. Yoshimine, in *Computational Methods for Large Molecules and Localized States in Solids*, edited by F. Herman, A. D. McLean, and R. K. Nesbet (Plenum, New York, 1973), p. 87; M. Yoshimine, J. Comput. Phys. **11**, 449 (1973).
[31]As a matter of fact, in a polyatomic problem, the diabatic quantity H_{ij} which appears in Eq. (5.2) is calculated for a particular cross section in the potential energy surface, and thus is expressed in the Nikitin representation. Hence, this quantity should be written H_{ij}. See Ref. 11 for a discussion of this point.
[32]The global functions reported in Figs. 13–16 have been calculated with the convention that g should always be positive.
[33]C. W. Gear, *Numerical Initial Value Problems in Ordinary Differential Equations* (Prentice Hall, New York, 1971).
[34]R. Bulirsch and J. Stoer, Num. Math. **8**, 1 (1966).
[35]We used Adams–Moulton and Bulirsch–Stoer subroutines kindly provided by Dr. C. Leforestier, and a Halton sequences generator written by Dr. S. Goursaud.
[36](a) X. Chapuisat, A. Nauts, and G. Durand, Chem. Phys. **56**, 91 (1981); (b) A. Nauts, thesis, Louvain-la-Neuve (1981).
[37]G. Herzberg, *Molecular Spectra and Molecular Structure* (Van Nostrand, Princeton, 1968), Vol. 2.
[38]R. J. Bartlett, I. Shavitt, and G. D. Purvis, J. Chem. Phys. **71**, 281 (1979).
[39]E. B. Wilson, J. C. Decius, and P. C. Cross, *Molecular Vibrations* (McGraw–Hill, New York, 1955).
[40]J. M. Hammersley and D. C. Handscomb, *Monte Carlo Methods* (Wiley, New York, 1964).
[41]J. H. Halton, Num. Math. **2**, 84 (1960).
[42]E. Wigner, Phys. Rev. **40**, 749 (1932).
[43]M. S. Bartlett and J. E. Moyal, Proc. Cambridge Philos. Soc. **45**, 545 (1949).
[44]E. J. Heller, J. Chem. Phys. **65**, 1289 (1976); **68**, 2066 (1978).
[45]F. Fiquet-Fayard, M. Sizun, and S. Goursaud, J. Phys. (Paris) **33**, 669 (1972).
[46]J. C. Lorquet, D. Dehareng, C. Sannen, and G. Raseev, J. Chim. Phys. Phys. Chim. Biol. **77**, 719 (1980); J. C. Lorquet, A. J. Lorquet, and M. Desouter-Lecomte, in *Quantum Theory of Chemical Reactions*, edited by R. Daudel, A. Pullman, L. Salem, and A. Veillard (Reidel, Dordrecht, 1980), Vol. II, p. 241; J. C. Lorquet, Org. Mass. Spectrom. **16**, 469 (1981).
[47]S. Chapman and R. K. Preston, J. Chem. Phys. **60**, 650 (1974); R. K. Preston, D. L. Thompson, and D. R. McLaughlin, *ibid.* **68**, 13 (1978).
[48]M. Baer, Chem. Phys. Lett. **35**, 112 (1975).
[49]M. Baer, Chem. Phys. **15**, 49 (1976).
[50]Z. H. Top and M. Baer, J. Chem. Phys. **66**, 1363 (1977); Chem. Phys. **25**, 1 (1977); M. Baer, Mol. Phys. **40**, 1011 (1980).
[51]X. Chapuisat and A. Naut, Chem. Phys. Lett. (to be published).
[52]M. Baer (private communication).
[53]H. G. Garnir, *Fonctions de Variables Réelles* (Vander, Bruxelles, 1970).